A Diagnostic Scheme for Separating Curvature and Along-Flow Speed Change Contributions to Middle Latitude, Synoptic-Scale Vertical Motions

by

Kathryn A. Abbott

A thesis submitted in partial fulfillment of

the requirements for the degree of

Master of Science

(Atmospheric and Oceanic Sciences)

at the

UNIVERSITY OF WISCONSIN - MADISON

2020

ABSTRACT

Mid-latitude synoptic-scale vertical motions arise from the vertical integral of divergent ageostrophic winds. For slowly evolving flows in the absence of friction, the ageostrophy is a result of accelerations associated with curvature and/or along-flow speed changes in the flow. Ageostrophy arising from curvature is oriented parallel to the flow while that arising from speed change is oriented perpendicular to it, thus raising the possibility that these separate contributions to divergent flow, and their attendant effects on ω, can be separated.

It is proposed that by identifying the along- and across-flow components of the ageostrophic wind, and subsequently computing ω from their respective divergences through vertical integration of the continuity equation, the total ω field can be partitioned into separate contributions physically attributable to the fundamental sources of ageostrophy – curvature and speed change. The nature of this proposition and of the resulting partitioned ω fields are examined through consideration of structural and dynamical aspects of an upper-level front from February 2018 and an explosive cyclone that occurred on the eastern seaboard of the United States in November 2018. The analysis reveals that the method does suggest physically reasonable results that may provide new insight into fundamental forcings for synoptic-scale vertical motions in a variety of canonical developmental environments.

ACKNOWLEDGEMENTS

Thank you to Dr. Jonathan Martin for providing me the opportunity to earn a graduate degree at the University of Wisconsin-Madison and for all of your support and advice throughout my time in the Atmospheric and Oceanic Sciences department. Being a member of the Martin Lab was an experience of a lifetime, and would not be complete without my fantastic officemates Maria Madsen and Patrick Beaty. Many thanks to you two for all of the laughs, advice, venting sessions, and for making 1421 a great place to be.

To the High Impact Weather Group, thank you for the abundant wealth of knowledge shared during our weekly meetings. It was always so enlightening to hear about the research being done throughout the 14th floor and beyond, as well as receive invaluable guidance on my own research. Special thanks to my committee members Dr. Stephanie Henderson and Dr. Michael Morgan for their insight not only during group meetings, but also while reviewing and commenting on my thesis as well.

There are so many other people from the department that have gotten me to where I am today. To all of the faculty, staff, and TAs who have supported my journey, thank you! To my undergraduate classmates Ryan, Josh, Nuo, Jenna, Matt, Toby, Zack, Peter, and Zach, getting through undergrad was truly a team effort in which I had the best teammates. You are all amazing!

Lastly, I could not have completed this degree without my personal support system. Thank you to my family, my partner Allie, and my friends near and far for your much needed support, guidance, and love in all of life's adventures.

TABLE OF CONTENTS

LIST OF FIGURES

LIST OF EQUATIONS

LIST OF ABBREVIATIONS

QG   **Q**uasi-**g**eostrophic

NWP   **N**umerical **w**eather **p**rediction

GEMPAK   **G**eneral **M**eteorological **A**nalysis **Pack**age

GFS-FNL   **G**lobal **F**orecast **S**ystem **fin**al analysis

PV   **P**otential **v**orticity

UTC   **C**oordinated Universal **T**ime

SLP   **S**ea **l**evel **p**ressure

1. INTRODUCTION

Perhaps no other basic state variable exerts a greater control on the sensible weather, and therefore has inspired more concentrated scientific investigation, than the vertical motion in the atmosphere. Indeed, assessment of synoptic-scale vertical motion is one of the most fundamental and important aspects of dynamic meteorology and its consideration has a rich history dating back to the early 20th century with compensation theory. This idea, articulated by Dines (1914), centers on the assertion that synoptic-scale vertical motions are the result of a significant difference between the lower-tropospheric and upper-tropospheric fields of divergence. Understanding of vertical motions hardly progressed for another two decades before Scherhag (1934) conceived of his "divergence theory" which proposed that "divergent upper winds must produce in general a fall of pressure if they are not compensated by a strong convergence below." By the end of the decade, Sutcliffe (1938, 1939) advanced these ideas through imposition of what would later be termed quasi-geostrophy. He noted that the departure from geostrophy was directly related to accelerations. Consequently, insight into the distribution of vertical motions could be gained by vertically integrating divergences which, in turn, implied that cyclone development could be forecasted by calculating the difference between divergence at the surface and upper levels. While these advancements in the first half of the 20th century were critical to advancing the field of synoptic meteorology, they all relied on assessment of the acceleration (i.e. divergence).

After the World War II, Sutcliffe's (1947) development theorem utterly transformed the thinking about synoptic scale vertical motions. Instead of relying on divergences, his development theorem diagnoses vertical motions through advection of vorticity by the thermal wind. This transformation depended upon the use of the vorticity equation and the geostrophic assumption but resulted in a conceptually elegant and operationally useful advance. This one idea completely changed the direction of vertical motion research - pushing it to the quasi-geostrophic (QG) diagnostic realm and away from a troubling reliance on calculating divergences from observed data. Adoption of this transition as convention was likely encouraged by the fact that at the time high-quality gridded observations of the winds, essential for accurate calculation of divergence, were unavailable.

Considerable refinement to Sutcliffe's original QG diagnostics have developed since 1947. Charney (1948) and Eliassen (1949) used Sutcliffe's work to catapult them towards developing a formal quasi-geostrophic theory in which realistic flow evolutions can be diagnosed by the geostrophic flow. Later, an approximate form of the QG omega equation (Bushby 1952) was derived that has since undergone many reformulations by Fjortof (1955), Thompson (1961), Petterssen (1962), and Eliassen (1962) to name a few. The QG omega equation does not depend on accurate wind observations and continues to be one of the leading methods for diagnosing synoptic-scale vertical motions. There are pitfalls to this diagnostic method, however, as rather large errors can occur near frontal regions and in the vicinity of rapidly deepening low pressure centers. Hoskins et al. (1978) introduced the Q-vector which is another QG formulation that has various

advantages, including retaining deformation as a forcing mechanism and computation of the forcing being local to a single isobaric level if desired. Using this diagnostic, one can simply look for regions of Q-vector convergence to diagnose ascent and Q-vector divergence to diagnose descent. Studies analyzing synoptic scale vertical motions continue to largely utilize QG theory in one form or another, with very little focus on the integrations of accelerations that preceded it.

In the modern era, the data limitations that fostered a QG approach to diagnosing vertical motions over the past 70 years have been relaxed and it is possible to consider the use of gridded model output as a direct input to the continuity equation. Returning to this framework by virtue of the routine availability of reliable wind data on mesoscale grids could foster new insights regarding the physical processes involved in the production of synoptic-scale vertical motions. This study attempts to do exactly that, and provides some new physical insights into the nature of synoptic-scale vertical motions.

These new insights rely heavily upon ageostrophic forcing associated with circulation patters around jet streaks and upper-level wave trains. Namias and Clapp (1949) and Bjerknes (1951) suggested that the geostrophic deformation present in the entrance and exit regions of a straight jet streak resulted in direct and indirect transverse circulations, respectively. Such transverse circulations occur from ageostrophy near the jet entrance region as the wind accelerates into the jet and the jet exit region as the flow slows when exiting the jet. This work resulted in the well known four-quadrant model of an upper level jet streak, illustrated in Figure 1.1a. Most

notably, the four-quadrant model shows ascent associated with the upper-level divergence in the right jet entrance and left jet exit regions, and decent associated with upper-level convergence in the left jet entrance and right jet exit regions. Upper-level wave trains possess their own ageostrophic wind fields arising from centripetal accelerations around troughs and ridges (Bjerknes and Holmboe 1944). In curved flow, the centrifugal force is always pointing away from the center of rotation. Thus, in the base of troughs the centrifugal force acts against the pressure gradient force, so the Coriolis force must decrease in order to achieve a balanced flow. Around ridges the centrifugal force acts in tandem with the pressure gradient force, thus an increase in the Coriolis force is required to achieve gradient balance. Therefore, flow around troughs is sub-geostrophic while flow around ridges is super-geostrophic, resulting in upper-level divergence and ascent downstream of upper-level troughs and convergence and descent upstream of upper-level troughs (Fig. 1.1b). The ubiquity of curvature and along-flow speed change in the middle and upper troposphere leads to ageostrophic circulations that can work independently, in tandem, or against each other to influence synoptic-scale vertical motions. Using model output alongside acceleration-based vertical motion diagnostics, we can separate components of ageostrophy that lead to such vertical circulations and compare these to the total vertical circulations from the model.

This thesis is organized in the following way. Chapter 2 will introduce an explanation of the methods used to retrieve partitioned vertical motion fields based on
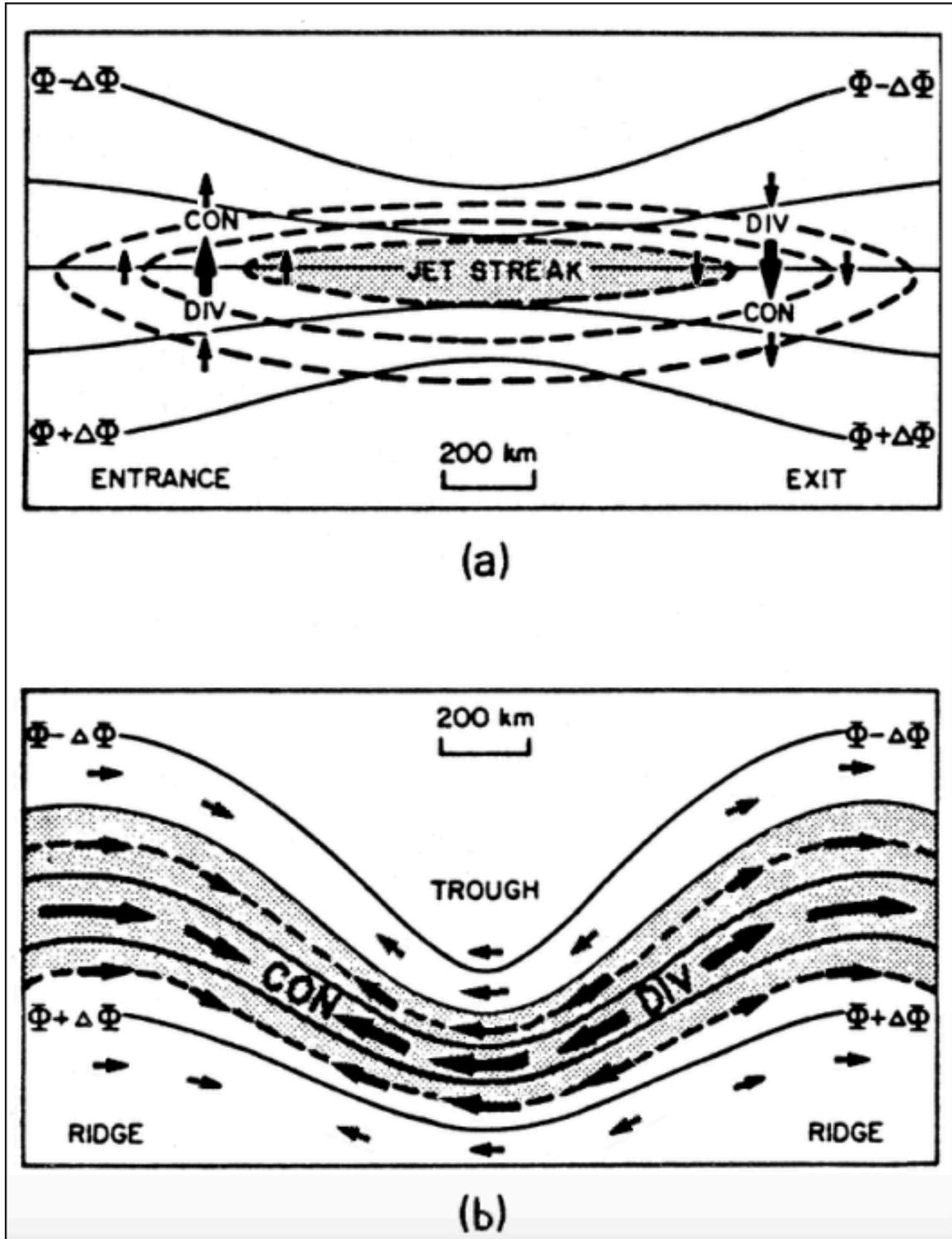
Figure 1.1: Schematic of ageostrophic motions (bold arrows) and convergence (CON) and divergence (DIV) fields associated with **(a)** a straight jet streak and **(b)** a synoptic wave train. The dashed lines are isotachs and the solid lines are geopotential height contours. From Shapiro and Kennedy (1981; Fig. 1).

the nature of the acceleration that leads to ageostrophy. In Chapter 3, the vertical

motion partition will be applied to an upper frontogenesis case that occurred over the

central United States on 2 February 2018. Chapter 4 will investigate explosive

cyclogenesis event that occurred off the Eastern Seaboard from 14-15 November 2018.

In Chapter 5, a summary of the results along with suggestions for future work will be

offered.

2. METHODS

An opportunity to investigate the production of synoptic-scale vertical motions outside of the quasi-geostrophic framework arises from consideration of the isobaric horizontal equation of motion:

$$\frac{d\vec{V}}{dt} = -\nabla\phi - f\hat{k} \times \vec{V} + \vec{F}$$

(1)

where ϕ represents isobaric geopotential, f is the Coriolis parameter, $\vec{V}$ is the horizontal velocity vector, and $\vec{F}$ is the friction vector. This equation dictates that a Lagrangian change in the wind vector will result from an imbalance between the pressure gradient, Coriolis, and friction forces. In this study we are concerned with the forcing of vertical motions in the middle and upper troposphere and so can simplify (1) by neglecting the friction term:

$$\frac{d\vec{V}}{dt} = -\nabla\phi - f\hat{k} \times \vec{V}$$

(2)

In the absence of friction, acceleration arises from imbalance between the pressure gradient and Coriolis forces and thus is physically linked to the ageostrophic wind. As suggested by Sutcliffe (1938), the mathematical connection is clear upon taking the vertical cross-product of (2);

$$\frac{\hat{k}}{f} \times \frac{d\vec{V}}{dt} = -\frac{\hat{k}}{f} \times \nabla\phi - \frac{\hat{k}}{f} \times \left(-f\hat{k}\right) \times \vec{V} = \vec{V} - \vec{V_g} = \vec{V_{ag}}$$

(3)

where $\vec{V_g}$ represents the geostrophic wind ($\frac{\hat{k}}{f} \times \nabla\phi$) and $\vec{V_{ag}}$ is the ageostrophic wind. Combining this expression with the isobaric continuity equation provides a direct link between the ageostrophic wind and the synoptic scale vertical motion since

$$\nabla \cdot \vec{V}_{ag} = \frac{-\partial \omega}{\partial p}$$

(4)

as the geostrophic wind is non-divergent on an f-plane. Acceleration of a vector is

associated with a change in its magnitude and/or its direction. In the case of the

horizontal (isobaric) wind, these conditions correspond to an along-flow change in

speed and/or a wind direction change. The canonical synoptic-scale features that

exhibit these characteristics are 1) jet streaks, and 2) mid-tropospheric waves (i.e.

troughs and ridges).

Figure 2.1 depicts the change in a wind vector (following an air parcel) over a

small time increment from t=0 to t=1. The difference between these vectors is the

acceleration following the parcel, $\frac{d\vec{V}}{dt}$. It is clear from the schematic that some portion of
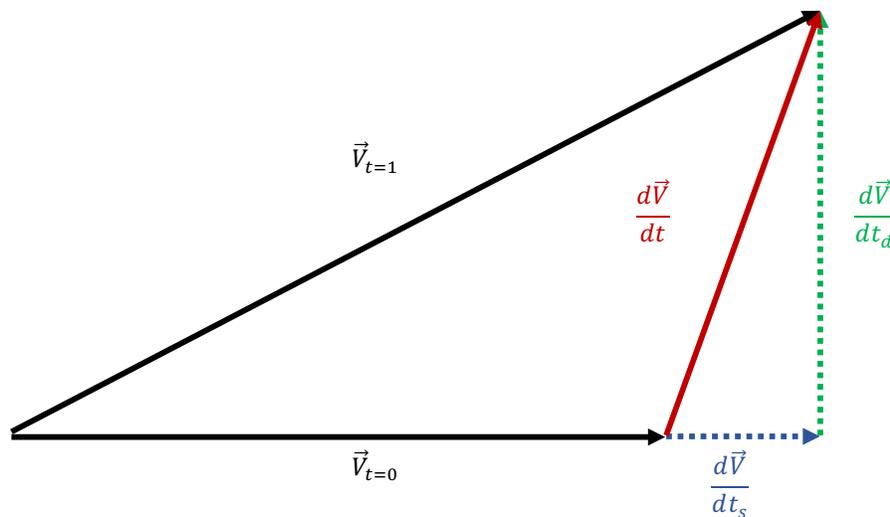
Figure 2.1: Diagram showing how the ageostrophic wind components are partitioned.

$\frac{d\vec{V}}{dt}$ accounts for the change in magnitude between *t*=0 and *t*=1 (labeled $\frac{d\vec{V}}{dt_s}$) while

another portion accounts for the change in direction (labeled $\frac{d\vec{V}}{dt_d}$). We will refer to

these two components of the actual acceleration vector as the speed change

component ($\frac{d\vec{V}}{dt_s}$) and the direction component ($\frac{d\vec{V}}{dt_d}$). It is clear that $\frac{d\vec{V}}{dt_s}$ will be directed

along the original flow direction ($\vec{V_t} = 0$) while $\frac{d\vec{V}}{dt_d}$ will be perpendicular to

it.

In the era of numerical weather predication (NWP), obtaining reasonably high

resolution, dynamically consistent gridded data sets is routine practice. Using such data,

one can calculate the ageostrophic wind at every grid point, can partition it into its

along- and across-flow components, and can then, as we will soon show, integrate the

isobaric continuity equation to obtain a calculated kinematic vertical motion field that

very closely approximates that calculated through numerical integration of the primitive

equations in the forecast model. In addition, following the just described method for

partitioning $\vec{V}_{ag}$, the total synoptic-scale omega field can likewise be partitioned into

separate pieces, physically tied to the effects of speed and direction change,

respectively- the most fundamental physical forcings for free atmosphere vertical

motions.

Integration of the isobaric continuity equation is performed using GDOMEG,

which is part of the suite of gridded data analysis tools in the General Meteorological

Analysis Package (GEMPAK, desJardins and Petersen 1983). GDOMEG employs an

O'Brien (1970) correction that includes setting vertical motion to zero at both the lowest

and highest pressure levels, represented by the dashed line in Figure 2.2.

The O'Brien correction is based on the solution of a variational problem which is

configured to minimize the squared difference between the model divergence and the

adjusted divergence while also satisfying the isobaric continuity equation subject to the

constraint of no vertical motion at 100 mb. The error in the divergence is assumed to

increase linearly with height. The goal of this adjustment is to nudge the vertical motion
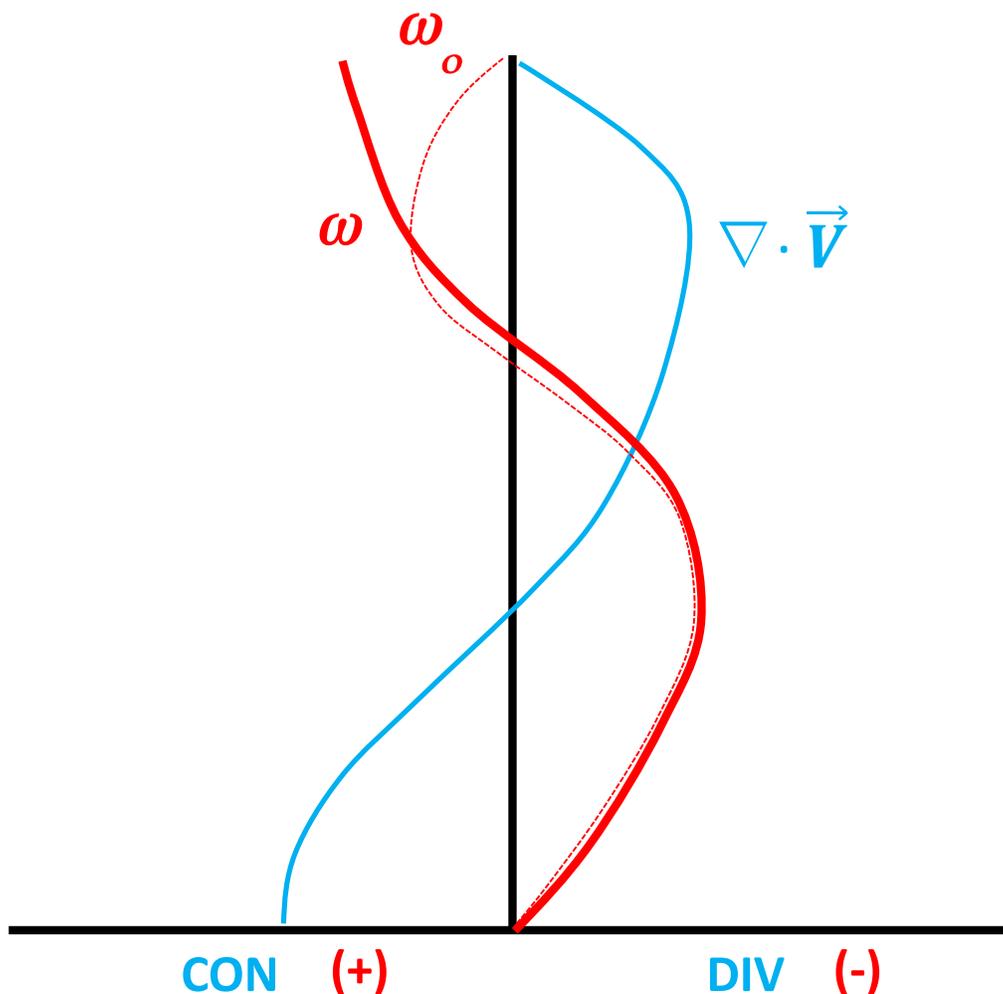
Figure 2.2: Diagram showing the relationship between the vertical distribution of divergences (solid blue line), the resulting vertical motion distribution (solid red line), and the vertical motion distribution with an O'Brien correction applied (dashed red line).

values at every level by a fraction of the excess omega at the top pressure level of 100 mb.

The results to be presented in this thesis will consist of a number of analyses of synoptic-scale vertical motion distributions associated with examples from a collection of canonical mid-latitude structures. In each such analysis, we first calculate the total column kinematic omega (using GDOMEG) by integrating the Global Forecast System Final analysis (GFS-FNL, NCEP 2007) at 1° x 1° horizontal grid spacing and 50 hPa intervals from 1000 to 100 hPa. We next isolate a frictionless layer, defined to extend from 800 to 100 hPa, and similarly calculate the kinematic omega in that layer. The omega in this layer is separable into the two pieces associated with speed change and direction change. In the integration of this frictionless layer we set the horizontal divergence equal to zero from 1000 to 800 hPa a suggested by the schematic in Fig. 2.3. Lastly, the 3D contribution to omega from the friction layer is recovered by subtracting the frictionless kinematic omega from the total kinematic omega. In the next chapter we more fully describe the data sets and individual cases employed in the analysis.
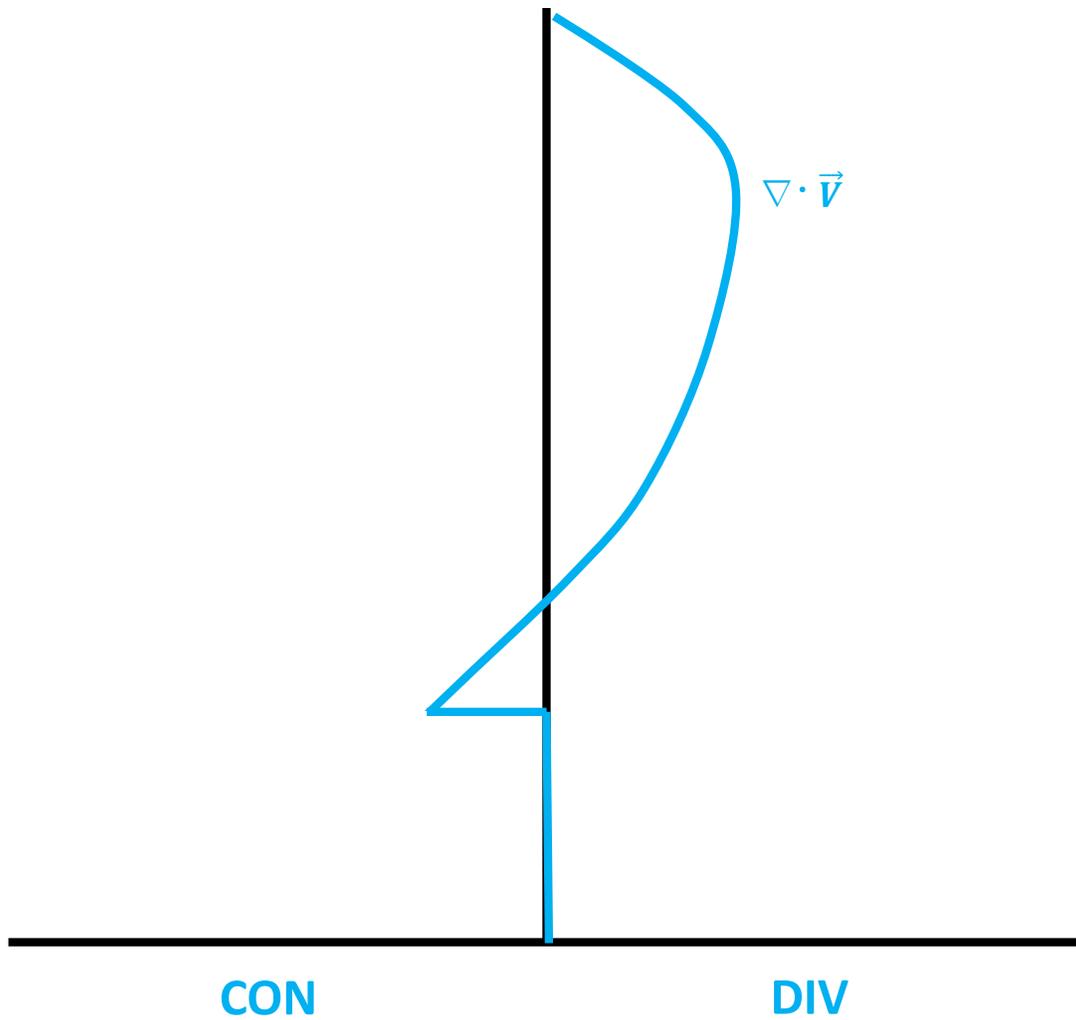
Figure 2.3: Diagram showing how the frictionless layer is defined with the blue line representing the vertical integration of the continuity equation.

3. UPPER FRONTOGENESIS CASE STUDY

3.1   Background

In 1922, Bjerknes and Solberg published the seminal work on mid-latitude cyclone structure and evolution that became known as the Norwegian Cyclone model. Central to the conceptual model was the notion of the characteristic fronts being knifelike, with a zero-order temperature discontinuities extending from the surface all the way to the top of the troposphere. The gradual introduction of routine upper-air analysis via soundings over the next two decades debunked this theory of frontal structure as the sounding data revealed that fronts are actually comprised of first-order discontinuities in temperature (Bjerknes 1926). This refinement deemphasized the frontal surface and led to adoption of the concept of a *frontal zone*. The first frontal zone detected at upper-levels was detailed by Bjerknes and Palmen (1937), citing sounding analysis that depicted baroclinic zones extending from the polar front that created a divide between warm, tropical air and cold, polar air through the whole of the troposphere. The upper region of this frontal zone revealed an S-shape fold in the tropopause.

Palmén took further interest in these features and continued to study them throughout the 1940's. In 1948 he noted that there was a middle-latitude belt of westerly jets that was the most pervasive feature of the 500 hPa flow. When comparing the jet features to the mean wind field, he found that they seemingly disappeared, leading to the hypothesis that they were a species of momentary features in the upper-tropospheric flow. Palmén (1948) also noticed that there was a strong temperature

gradient that moved with these westerly jet features and suggested the horizontal

baroclinic zones and jet features at 500 hPa occurred simultaneously and were the

result of the same process. Furthermore, he proposed this process resulted from a

cross-stream vertical circulation around the zonal jet features.

Palmén and Nagler (1949) gave the first detailed description of the three-

dimensional synoptic structure of the disturbances being observed in the 500 hPa

westerlies. In their analysis they determined that 50 percent of the equator to North

Pole temperature difference was located within a 1000 km band in the mid-latitudes,

lending further evidence that these mid-tropospheric features were, in fact, classifiable

as frontal zones. In their study they also determined that the upper-frontal zones were

not formed by temperature changes arising from horizontal advection, but instead from

vertical displacements along the flow's trajectory. They concluded that the flow

descended from ridges to troughs and ascended when moving from troughs to ridges.

On the basis of Palmén and Nagler's findings, many in the field sought to

understand the physical processes which resulted in upper-frontogenesis. Reed and

Sanders (1953) showed the need for a cross-stream gradient of sinking air which helps

intensify the horizontal temperature gradient via adiabatic warming of the warm air

side. Potential vorticity (PV) analysis conducted by Reed (1955) found that the upper-

frontal zone also consists of a thin wedge of stratospheric air, identified by its large

values of PV, that descend into the lower levels of the troposphere, sometimes reaching

as low as 700 to 800 hPa. Another key developmental feature of upper fronts identified

by Mudrick (1974) in his idealized modeling study of the growth of baroclinic waves is

that they have a tendency to form in regions of geostrophic cold air advection in

northwesterly flow along the jet axis. Shapiro (1981, 1983) took a different approach

and studied the effects of confluence and horizontal shear on upper frontogenesis using

the Sawyer (1956)-Eliassen (1962) equation. He found that the geostrophic cold air

advection acts to displace the thermally direct circulation from the confluent jet

entrance region, placing the subsiding branch on the warm side of the baroclinic zone to

induce a thermally indirect circulation. Together, all of these findings lead to the

synoptic environment of an upper-level front. One forms most optimally in a region of

geostrophic cold air advection along the jet axis, which leads to a thermally indirect

circulation on the cyclonic shear side of the jet, allowing for maximum subsidence near

the jet core to occur.

3.2   Synoptic Overview

On 2-3 February 2018 upper-level frontogenesis occurred across the Plains and

the Midwest of the United States. The development involved subduction of

stratospheric air with high potential vorticity into the middle and upper troposphere

while intensifying a strong jet streak amid a broad upper-level trough in the

development environment. First, the development of the upper-level front will be

presented via a synoptic overview. Next, the vertical motion partition will be applied

during the period of strongest descent of stratospheric air into the troposphere. This

analysis will assist in the formulation of key takeaways from the application of the

vertical motion partition to upper-level frontogenesis.
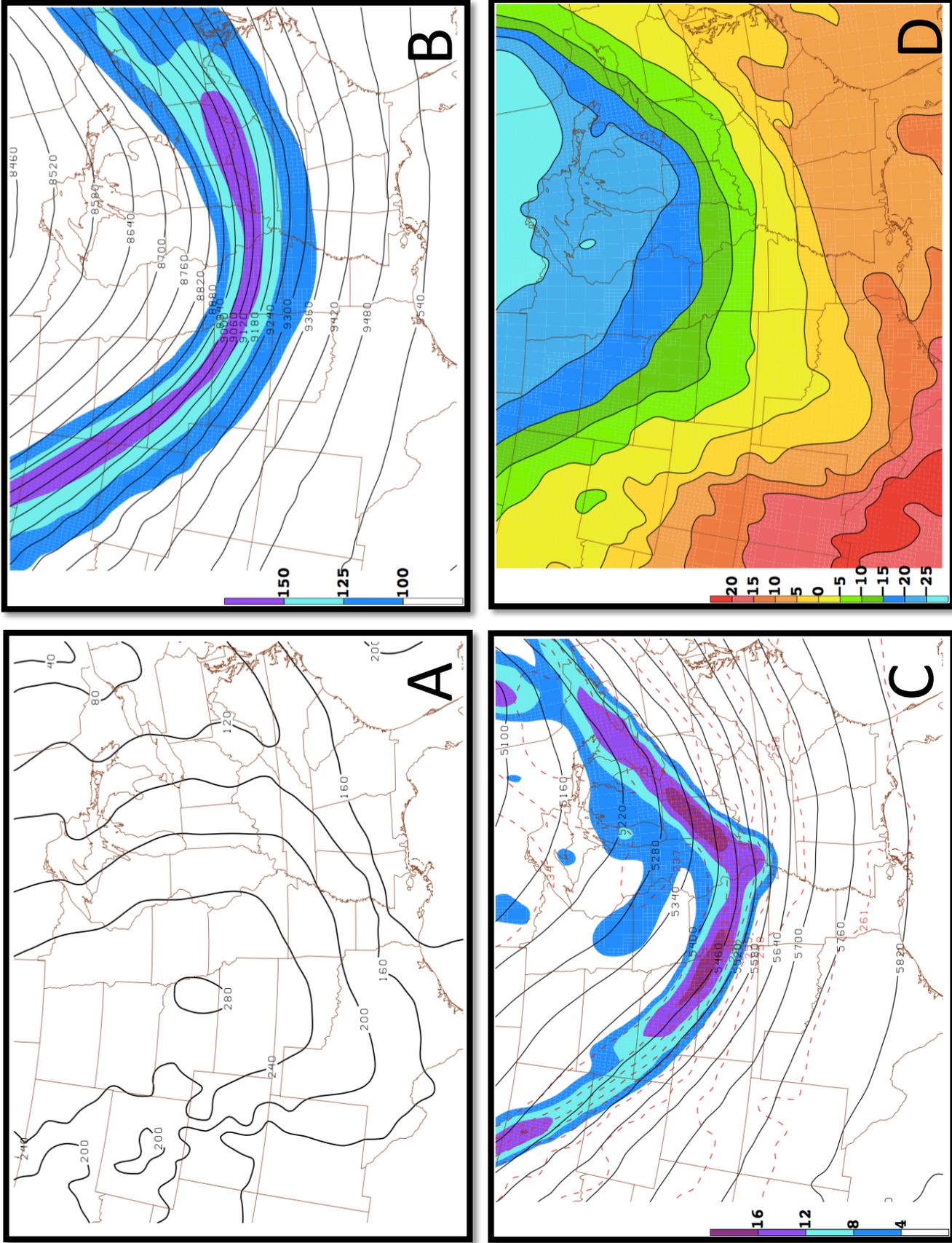
Figure 3.1: **(A)** 1000 hPa heights (black) every 40 m, **(B)** 300 hPa heights (black) and wind in knots (color fill), **(C)** 500 hPa heights (black), temperature every 3 degrees Kelvin (dashed contours), and positive vorticity (color fill), and **(D)** 850 temperatures (color fill) all from 00 UTC on 02 February 2018.

At 0000 Universal Time Convention (UTC) 2 February 2018 synoptic characteristics consistent with upper-level frontogenesis were emerging over the central United States. At this time, an anticyclone with a maximum 1000 hPa height of 280 meters (equivalent to a sea level pressure (SLP) of ~1035 hPa) was centered over eastern Nebraska (Fig. 3.1a). At 300 hPa (Fig. 3.1b) a very broad upper-level trough with its base located near southern Illinois stretched across the entire eastern two-thirds of the United States. An elongated jet streak with core speeds near 150 knots was situated within that wave, mostly on the upstream side of the trough. The same broad trough was evident in the height field at 500 hPa (Fig. 3.1c). More noticeably, a V-shaped region of positive vorticity was centered just west of the base of the trough. Along the positive vorticity strip upstream of the trough axis a strong middle-troposphere temperature gradient was present characterized by slight geostrophic warm air advection over parts of Montana and Wyoming and nearly neutral temperature advection further downstream. On the downstream side of the trough there was geostrophic cold air advection. At 850 hPa (Fig. 3.1d) the baroclinicity beneath the upstream side of the upper-level trough was not strong. Instead, the thermal contrast was strongest in the region of 500 hPa cold air advection downstream of the trough across the northeastern states.

By 1200 UTC 2 February 2018, the 1000 hPa height maximum had intensified slightly and was centered over western Missouri (Fig. 3.2a). The wind speed maximum remained near 150 knots at 300 hPa (Fig. 3.2b). The upper-level trough within which the
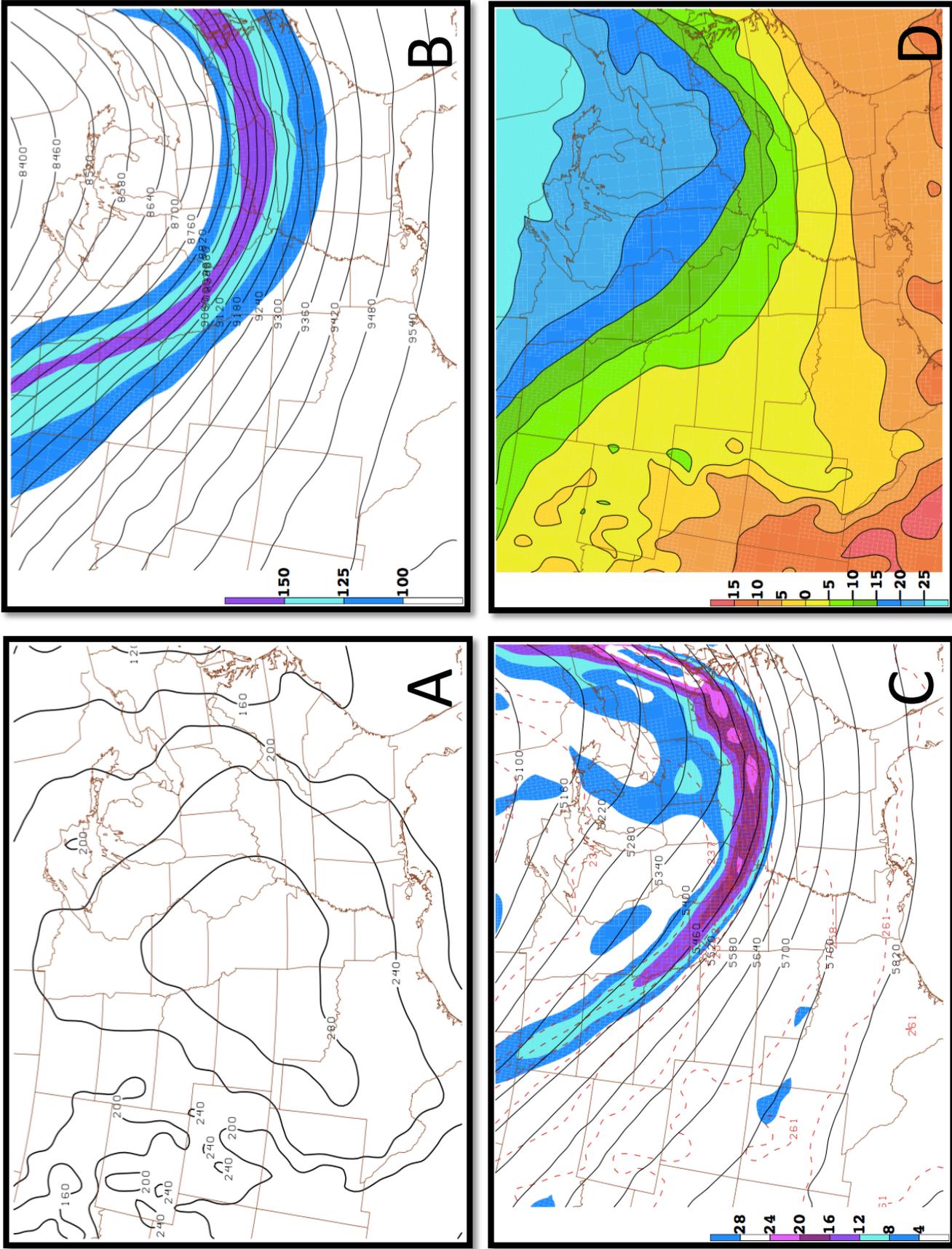
Figure 3.2: (A) 1000 hPa heights (black) every 40 m, **(B)** 300 hPa heights (black) and wind in knots (color fill), **(C)** 500 hPa heights (black), temperature every 3 degrees Kelvin (dashed contours), and positive vorticity (color fill), and **(D)** 850 temperatures (color fill) all from 12 UTC on 02 February 2018.

speed maximum was embedded had intensified becoming slightly more curved with its base located near the Kentucky-Tennessee border. At 500 hPa the positive vorticity strip had intensified into a U-shaped feature aligned parallel with the height lines upstream of the trough axis (Fig. 3.2c). Most notably, strong geostrophic cold air advection extended from northeast Missouri eastward to central Virginia as the baroclinic zone had intensified at 500 hPa. Meanwhile, at 850 hPa, the baroclinic zone had not changed in intensity much while it progressed eastward (Fig. 3.2d)

Twelve hours later, at 0000 UTC 3 February 2018, the broad anticyclone had weakened slightly as it moved southeastward (Fig. 3.3a). The upper-level trough continued to intensify, exhibiting more curvature at 300 hPa by this time as the jet streak progressed downstream of the sharper trough axis (Fig. 3.3b). The trough at 500 hPa had evolved in a similar manner resulting in a strong, linear vorticity strip on the downstream side of the 500 hPa trough axis by this time (Fig. 3.3c). The region of geostrophic cold air advection upstream of the trough axis that had been so apparent at the prior time it had almost disappeared by 0000 UTC 3 February. The 850 hPa baroclinic zone continued to make eastward progress without much alteration in the details of its structure (Fig. 3.3d).

3.3   Analysis and Results

In order to look at the vertical motions associated with this upper front, a cross section was taken from point A to point B on 1200 UTC 2 February 2018, through the core of the jet and strong baroclinic zone, as shown in Fig. 3.4. The cross section reveals a nicely defined extrusion of stratospheric air (characterized by high PV) into the middle
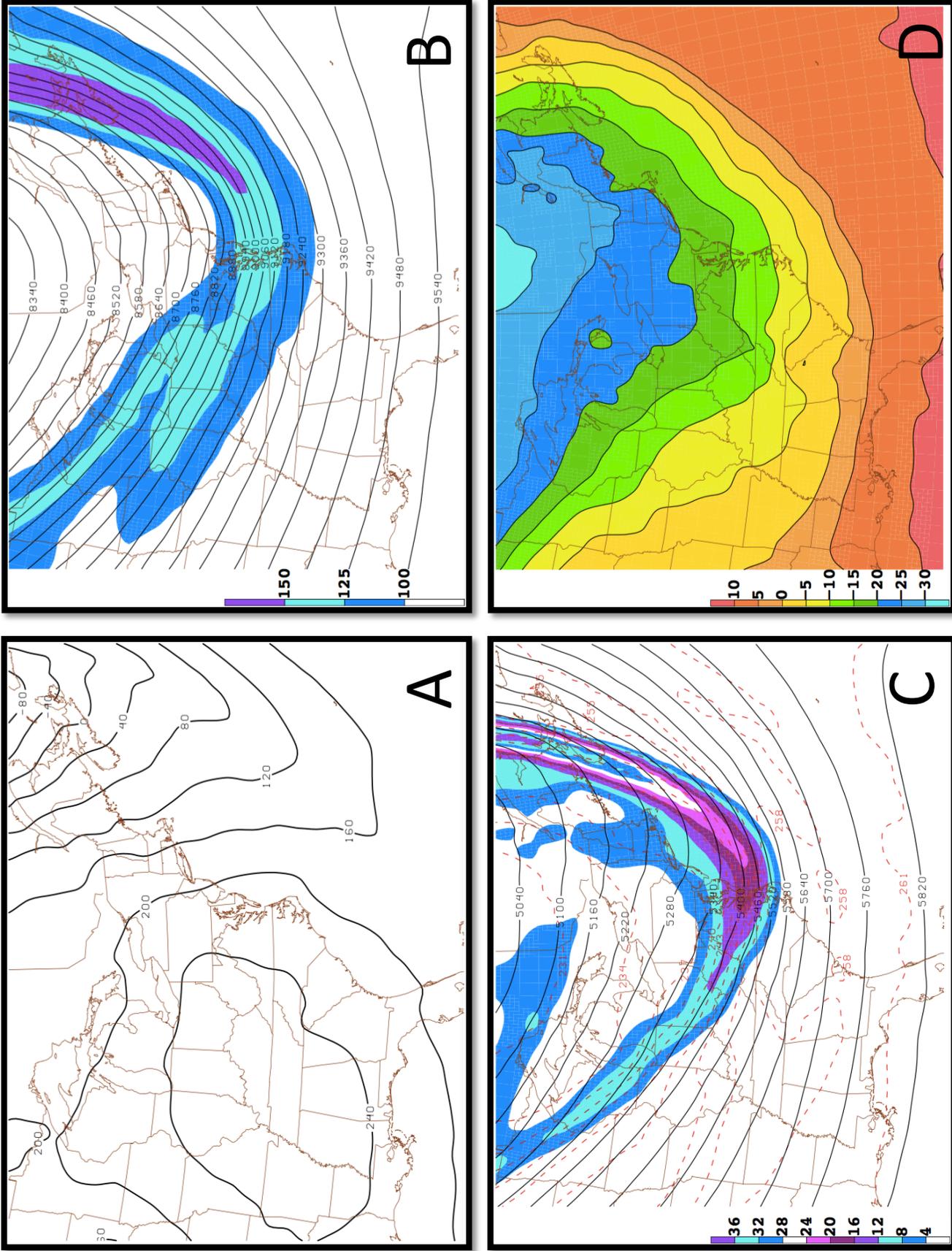
Figure 3.3: (A) 1000 hPa heights (black) every 40 m, **(B)** 300 hPa heights (black) and wind in knots (color fill), **(C)** 500 hPa heights (black), temperature every 3 degrees Kelvin (dashed contours), and positive vorticity (color fill), and **(D)** 850 temperatures (color fill) all from 00 UTC on 03 February 2018.
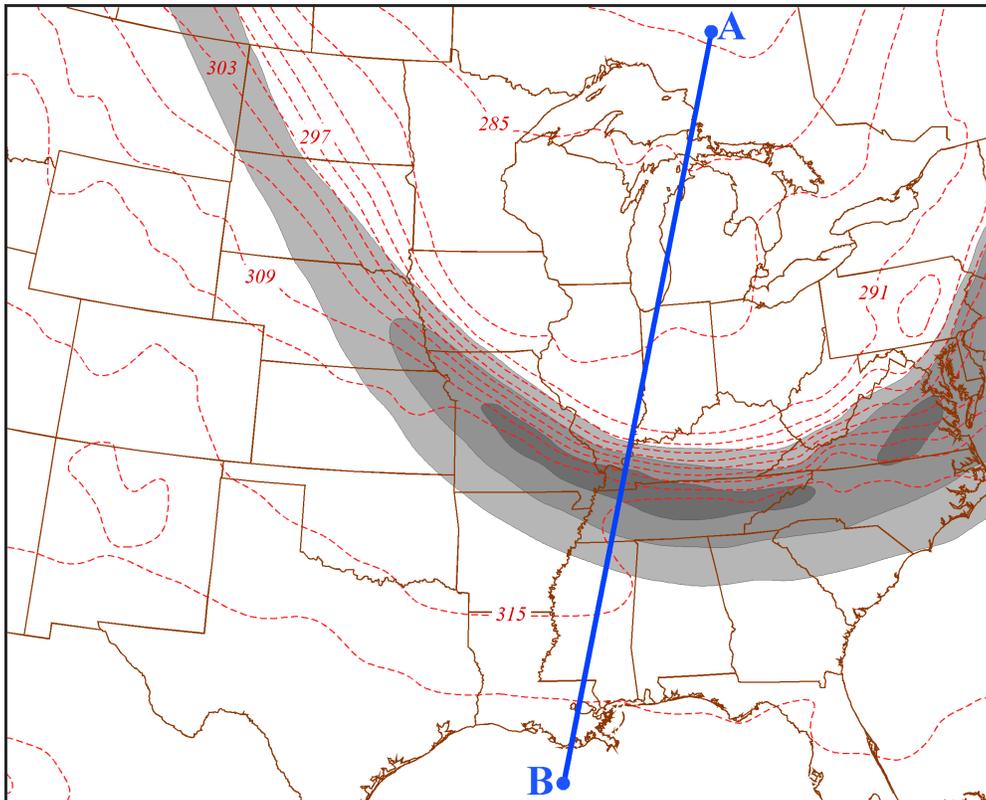
Figure 3.4: Diagram showing where the cross sections used in this analysis section were taken from point A-B, with theta in red and wind speed shaded in grey.
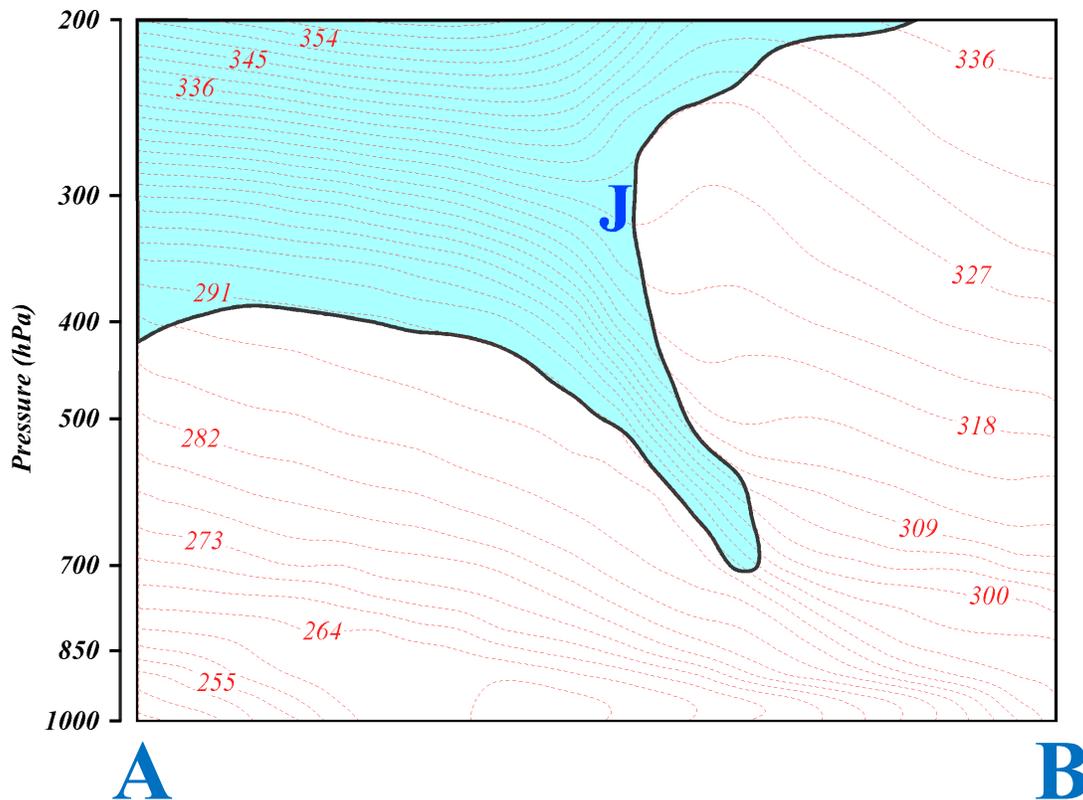
Figure 3.5: Theta (red) and PV (shaded blue, greater than 1 PVU) along line A-B, with the core of the jet labeled 'J'.

and upper troposphere (Fig. 3.5). Because such a PV tendril is drawn down into the

troposphere by subsidence on the anticyclonic shear side of a jet streak (Keyser and

Shapiro 1986, Rotunno et al. 1994, Martin 2014), the foregoing examination will focus

on middle and upper tropospheric descent in the upper-level front environment. Figure

3.6a illustrates the GFS model subsidence associated with this upper front. Broad

subsidence is centered beneath the jet core in accord with theoretical expectations

based on application of both the quasi-geostrophic (Martin 2014) and semi-geostrophic

(Shapiro 1981) perspectives of vertical motion forcing. This region of subsidence is
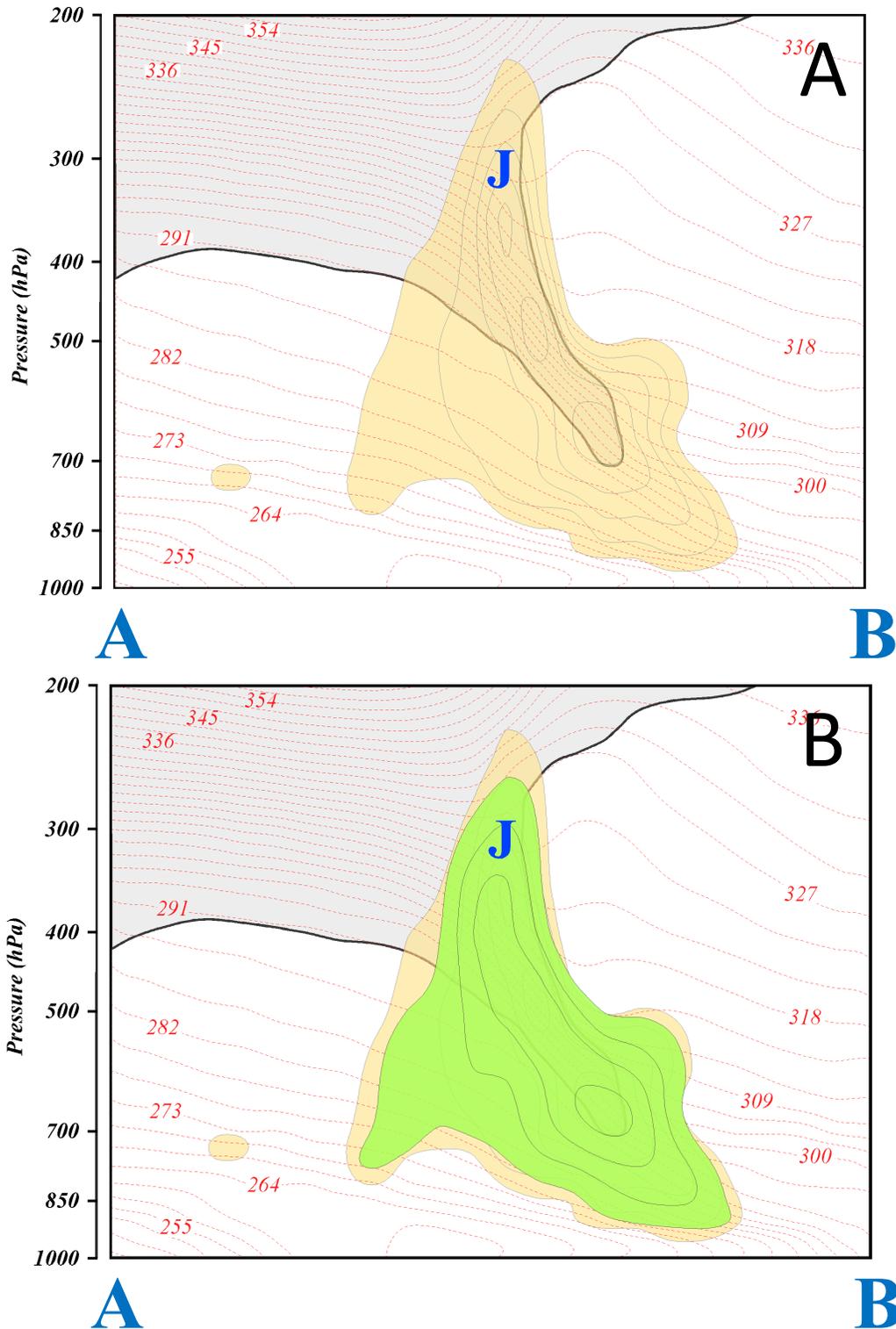
Figure 3.6: Cross section of theta (red) and PV (shaded grey, greater than 1 PVU) along line A-B of **(A)** 00h forecast of GFS model vertical motion (only subsidence is shown, every μ bar s-1, starting at -2 μ bar s-1) and **(B)** Kinematic vertical motion (subsidence only) from the integrated ageostrophic divergence from the GFS (green shading, every μ bar s-1, starting at -2 μ bar s-1).

faithfully reproduced by the total kinematic subsidence calculated using the O'Brien method (Fig. 3.6b).

Kinematic subsidence forced by boundary layer friction (in which the boundary layer is defined from 1000 to 800 hPa) is shown in the yellow shading in Fig. 3.7a, indicating that some small fraction of the total subsidence is frictionally induced. The "free atmosphere" kinematic subsidence from 800 to 100 hPa is portrayed in Fig. 3.7b. Most of the kinematic descent forced in the prescribed boundary layer is found below 500 hPa while descent forced in the free atmosphere is largely located between 700-300 hPa. A comparison of the two plots in Fig. 3.7 reveals that there are areas of ascent forced by the upper and lower troposphere that act independently, such as the upper and lower tropospheric regions, while other areas of ascent, namely in the middle troposphere, experience ascent forced in both the boundary layer and the free atmosphere.

The frictionless kinematic omega is the sum of components arising from speed change and curvature. The subsidence forced by speed change from the across-flow ageostrophic wind is shown in Fig. 3.8a. This component has a strong signal – in fact, the speed change subsidence is larger than the total upper tropospheric subsidence while covering almost the entire region of subsidence. The subsidence forced by direction change (Fig. 3.8b) has a much weaker signal but nonetheless helps contribute to the total kinematic subsidence, especially near the base of the upper front. The predominance of the speed change component of ascent as compared to the directional change component makes physical sense in regard to the synoptic environment of this
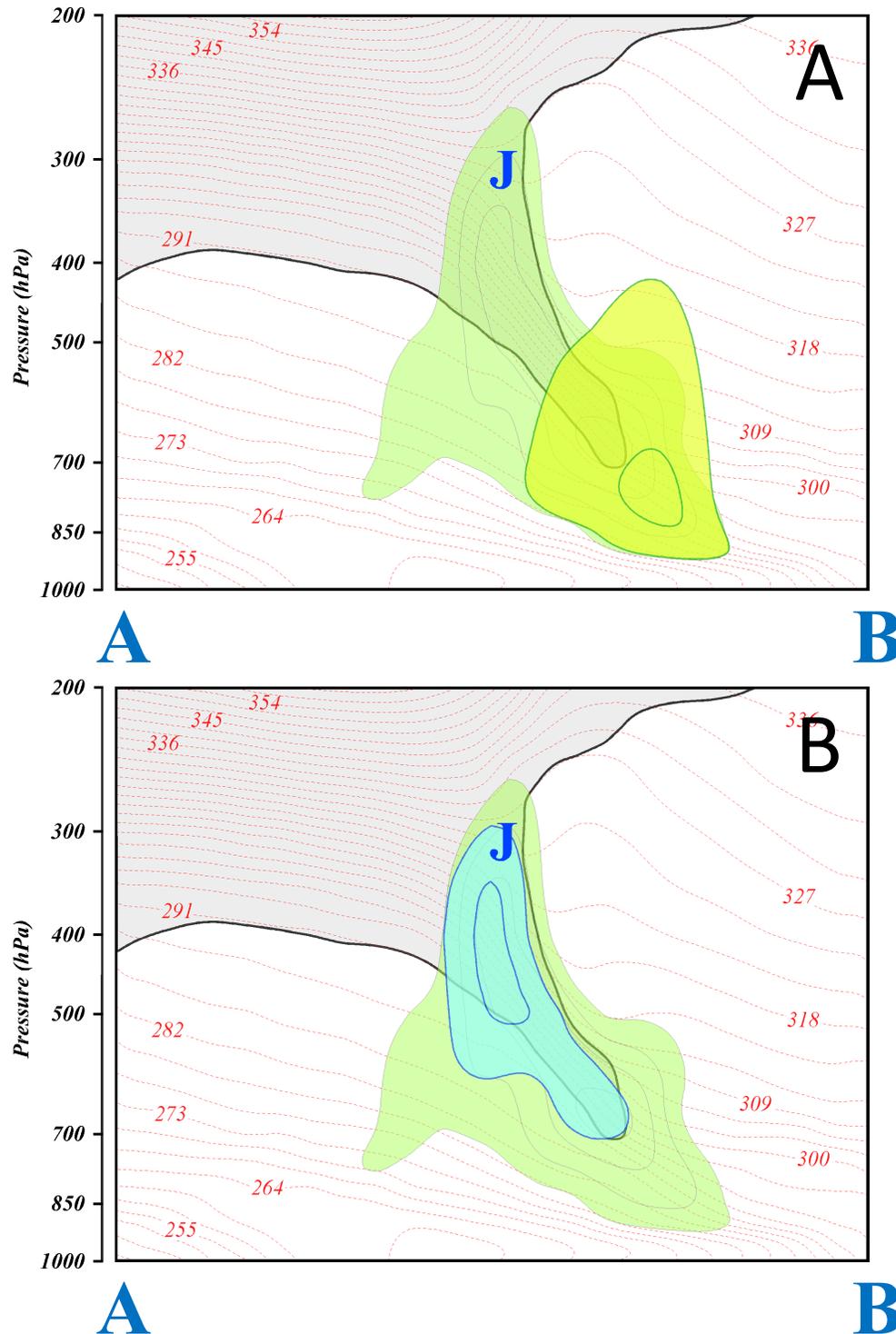
Figure 3.7: Cross section of along line A-B of **(A)** Yellow shading is the kinematic omega forced by ageostrophic divergence in the boundary layer (1000 to 800 hPa) every μ bar s-1 starting at 2 μ bar s-1 **(B)** Kinematic omega (subsidence only) forced by upper tropospheric, frictionless ageostrophic flow (blue shading) every μ bar s-1 starting at 2 μ bar s-1.
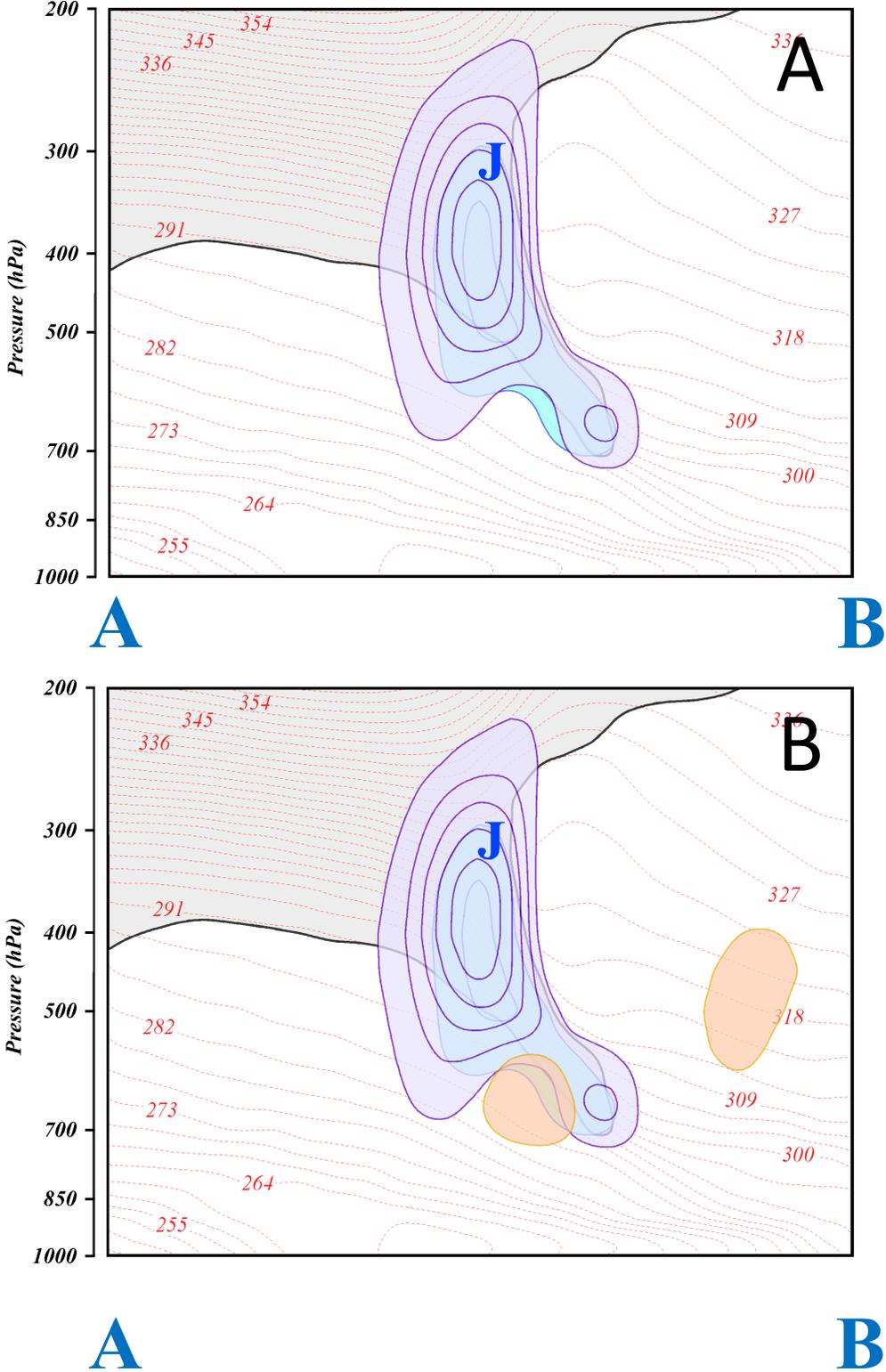
Figure 3.8: Cross section along line A-B of upper tropospheric kinematic omega (subsidence only) forced by **(A)** speed change component of the ageostrophic wind (purple shading) and **(B)** directional change component of the ageostrophic wind (orange shading) every μ bar s-1 starting at 2 μ bar s-1.
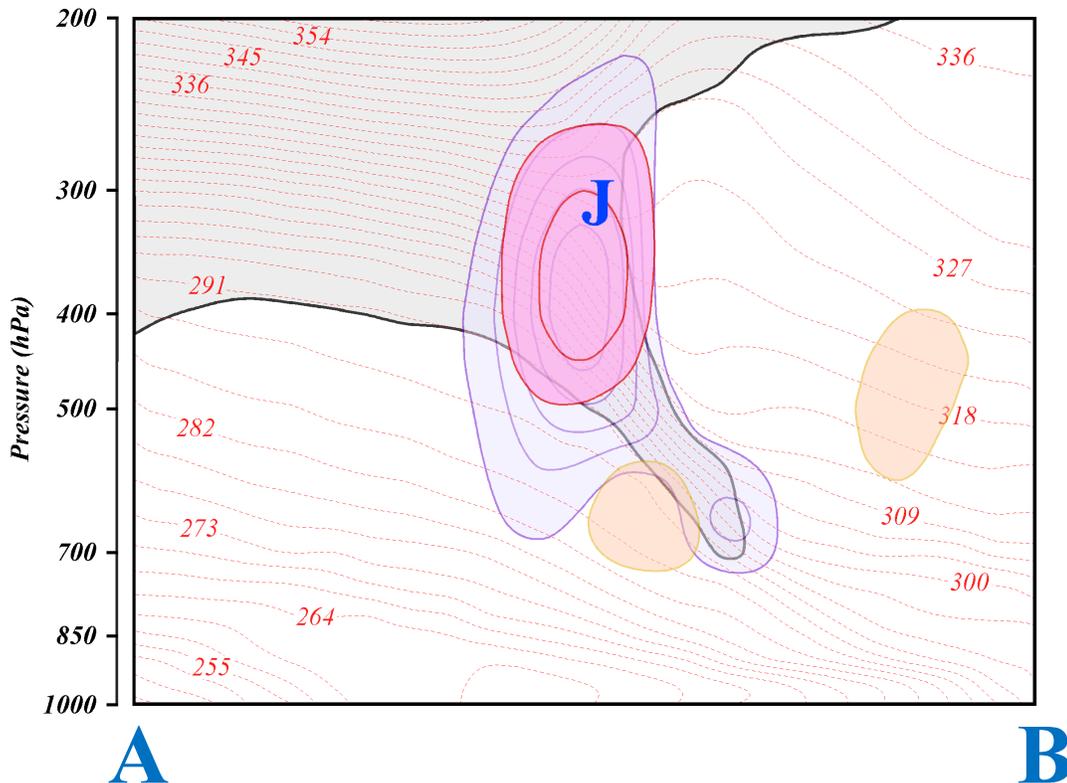
Figure 3.9: Same as Figure 3.8 with pink shading (ascent only) forced by direction change component of the ageostrophic wind every μ bar s-1, starting at 1 μ bar s-1.

upper-level front. While the cross section through the upper front is located slightly upstream of the upper-level trough, the trough is very broad so the ageostrophy associated with directional changes of the flow are minimal compared to those being generated by speed change ageostrophy from the roaring jet in this case. Magnitude differences aside, why is the subsidence of both components illustrated in Fig. 3.8b much larger in magnitude and area than the total kinematic subsidence?

One must also consider ascent in the region as well, and when ascent in the upper troposphere caused by a directional change Is added, it is clear that it directly opposes the speed change descent (Fig. 3.9) near the core of the jet. In the horizontal environment we see a similar signal. Plotted in Fig. 3.10a is the kinematic subsidence
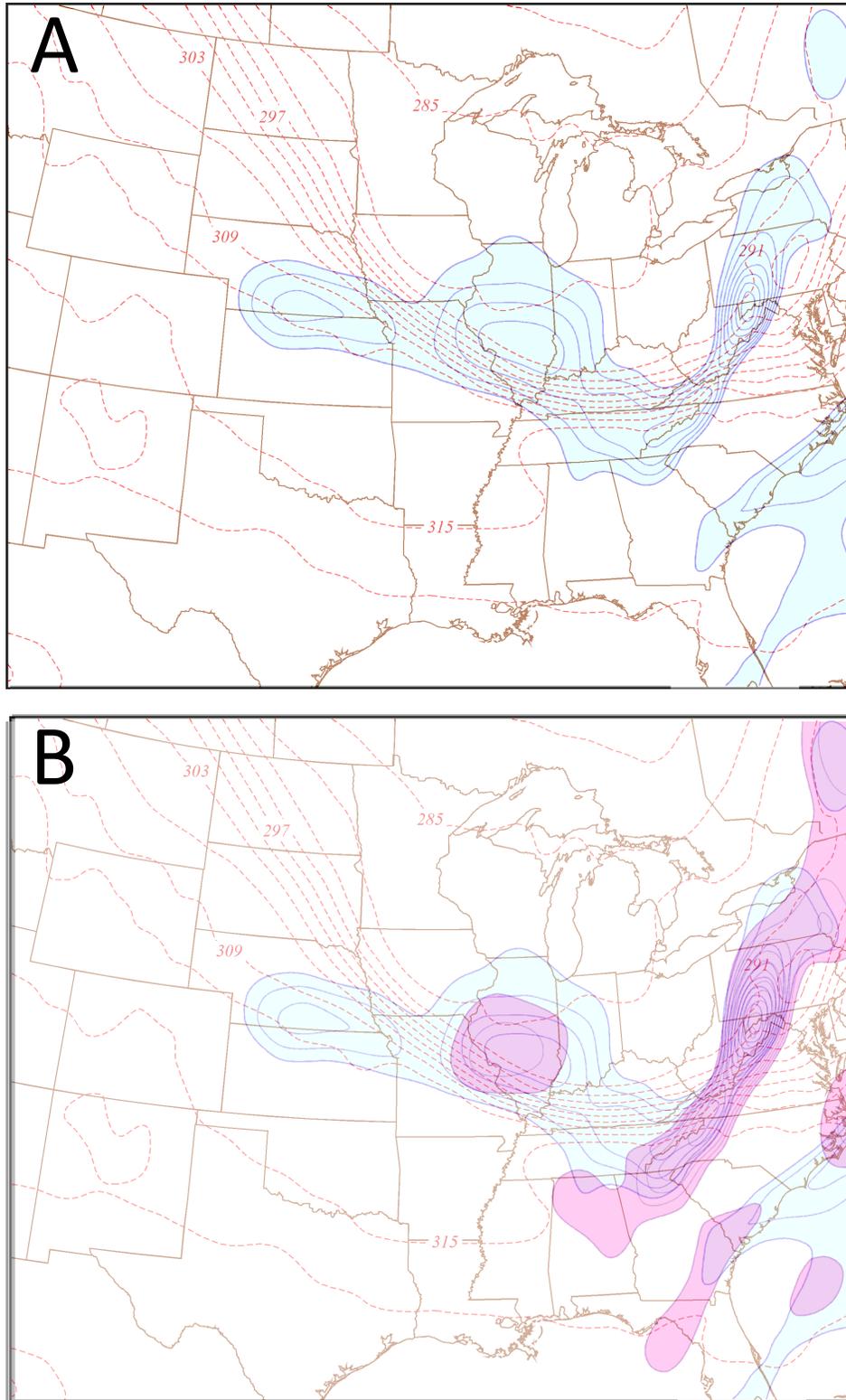
Figure 3.10: 500 hPa theta (red) with **(A)** kinematic subsidence in the upper-troposphere from speed change ageostrophy in blue and **(B)** same as (A) with ascent from directional change ageostrophy in purple.

resulting from speed change. Mirroring what was seen in the vertical, the speed change

descent is strongly opposed and sometimes overpowered by ascent arising from

directional changes, especially downstream of the broad upper level trough (Fig. 3.10b).

Note the cancelation of these vertical motions along the spine of the Appalachians. This

tug of war between ascent and descent after partitioning the upper-tropospheric

vertical motion fields has proven to be quite puzzling when trying to determine the

significance of the partitioned vertical motion fields. One cannot only rely on the speed

change and directional change partitioned ascent or descent to conduct a

comprehensive analysis, but instead must look at partitioned regions of ascent, descent,

and their interaction with one another in order to resolve the full partitioned

environment.

4. CYCLOGENESIS CASE STUDY

On 14-15 November 2018 explosive cyclogenesis occurred along the east coast of North America. The cyclone underwent over 44 hPa of deepening from 0000 UTC 14 November 2018 to 0000 UTC 15 November 2018. This cyclone is of particular interest for the current study as a consequence of the coexistence a strong jet streak and upper-level trough in the development environment. First, we will detail the synoptic environment of the object cyclone in question in a synoptic overview. Next, the vertical motion partition and analysis will be applied during the period of most rapid intensification. This analysis will assist in the formulation of key takeaways from the application of the vertical motion partition to a middle-latitude cyclone.

4.1   Synoptic Overview

At the beginning of rapid intensification at 0000 UTC on 14 November 2018 (Fig. 4.1) the cyclone center was located between the Gulf of Maine and the Bay of Fundy along the coasts of Maine, New Brunswick, and Nova Scotia and had a minimum sea-level pressure of 0 meters at 1000 hPa (e.g. a sea-level pressure minimum of 1000 hPa) (Fig. 4.1a). At 300 hPa (Fig. 4.1b) the flow was very wavy with three distinct troughs in the domain. The trough of interest, with its axis centered over Lake Huron, was the western member of an extended wave train stretching from eastern Ontario to the central north Atlantic. There was a strong upper-level jet streak with maximum speeds over 200 knots stretching from the base of the trough in Indiana to New Brunswick. A geopotential height minimum of 8460 meters was centered over Hudson Bay. The 500
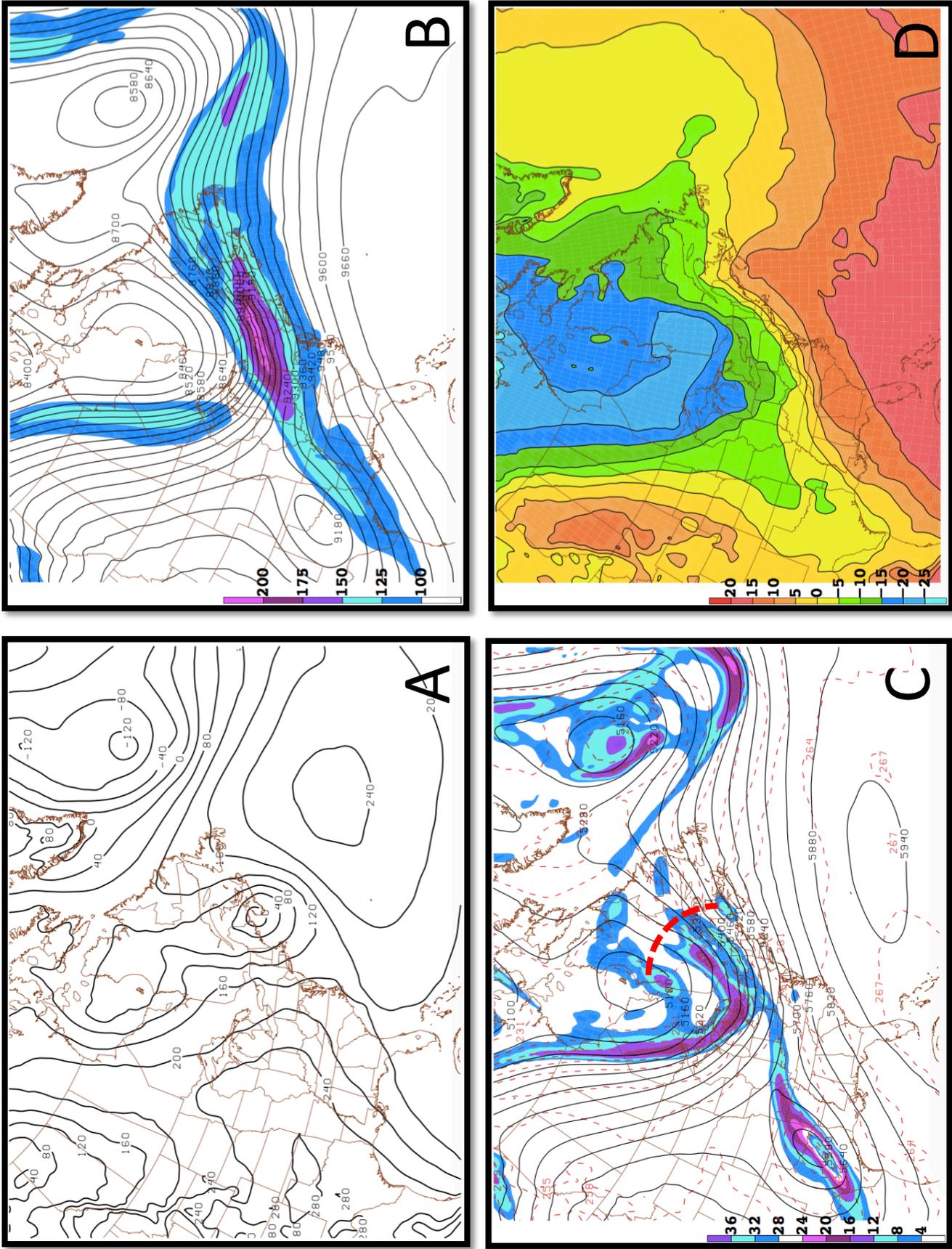
Figure 4.1: **(A)** 1000 hPa heights (black) every 40 m, **(B)** 300 hPa heights (black) and wind in knots (color fill), **(C)** 500 hPa heights (black), temperature every 3 degrees Kelvin (dashed contours), and positive vorticity (color fill) with inflection point (red), and **(D)** 850 hPa heights (black) and temperatures (color fill) all from 00 UTC on 14 November 2018.

hPa geopotential height distribution was broadly similar with a minimum of 5100

meters over James Bay (Fig. 4.1c). There was a positive vorticity streamer stretching

from well upstream of the trough axis, through its base and then extending downstream

into central Quebec. At 850 hPa, the strongest baroclinic zone stretched

southwestward from southern Quebec to eastern Kentucky and represented the cold

front of the developing cyclone (Fig. 4.1d). A weaker, less well organized warm frontal

baroclinic zone extended to the east of the low pressure center across Maritime

Canada.

By 1200 UTC 14 November 2018 the minimum 1000 hPa geopotential height of

the cyclone had deepened to -200 m (a roughly 25 hPa decrease of SLP) and had tracked

northeastward into the Gulf of St. Lawrence (Fig. 4.2a). The development occurred

throughout the troposphere as the 300 hPa geoptential minimum fell by 60 m to 8400

meters with an enhancement to the flow's curvature downstream of the trough as a

result of amplification of the downstream ridge (Fig. 4.2b). The core of the jet had

weakened slightly by this time but was still roaring at just over 200 knots. The horizontal

extent of the jet had not changed substantially (it now extended from Pennsylvania to

Newfoundland) but it had acquired a greater curvature within the base of the trough. At

500 hPa it was not height falls but vorticity increase that marked the greatest change in

the 12h interval (Fig. 4.2c). Though the positive vorticity feature was still predominantly

streamer-like in shape, its leading end had strengthened and dramatically begun to ball

up in the Gulf of St. Lawrence. The cold frontal baroclinic zone at 850 hPa remained
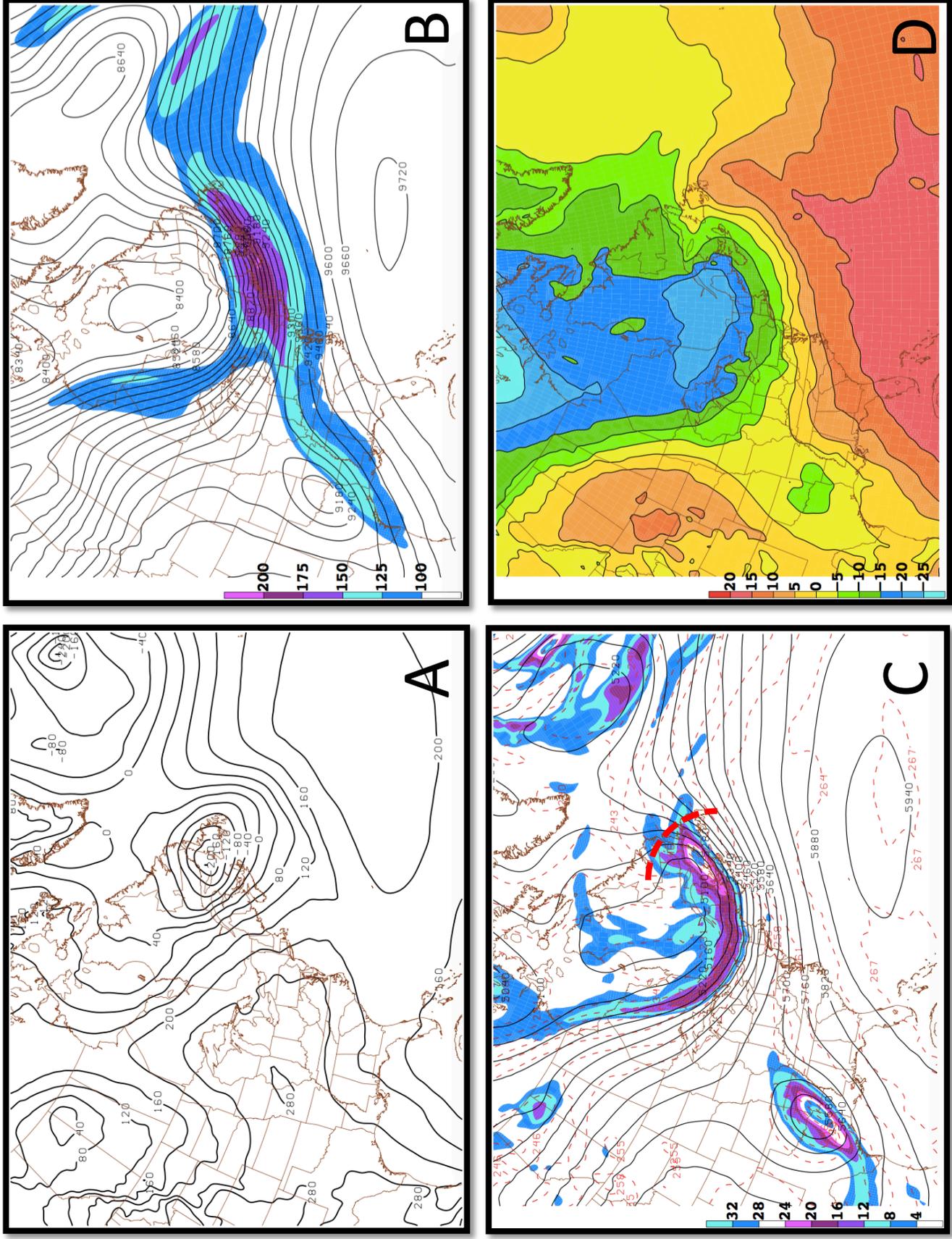
Figure 4.2: (A) 1000 hPa heights (black) every 40 m, **(B)** 300 hPa heights (black) and wind in knots (color fill), **(C)** 500 hPa heights (black), temperature every 3 degrees Kelvin (dashed contours), and positive vorticity (color fill) with inflection point (red), and **(D)** 850 temperatures (color fill) all from 12 UTC on 14 November 2018.

strong while a robust thermal ridge had developed that connected the triple point to the cyclone center as is characteristic of occluded cyclones (Fig. 4.2d).

In the subsequent 12 hours the cyclone underwent another period of extraordinarily rapid intensification, as the 1000 hPa geopotential height minimum dropped another 175 m (~22 hPa of SLP) while the cyclone continued to track to the northwest finding itself centered off the southeast coast of Labrador by 0000 UTC 15 November (Fig. 4.3a). At 300 hPa the geopotential height maximum remained at 8400 meters as the jet core strengthened slightly while maintaining core speeds over 200 knots (Fig. 4.3b). The most notable transformation occurred at 500 hPa where heights fell 180 meters to 4920 meters at the core of the upper level low (Fig. 4.3c). The positive vorticity feature had, by this time, become much more balled up at the leading edge of the streamer and had begun to wrap around the central vortex. This transformation, coupled with the extension of the occluded thermal ridge noted at the prior time, was evidence of a robustly occluded middle-latitude cyclone that had likely reached, or just surpassed, its period of most rapid development (Fig. 4.3d). The temperature gradient along the cold front had weakened slightly and the warm front remained rather stubby.

4.2   Analysis and Results

The foregoing synoptic overview of the cyclone in question suggests that 1200 UTC 14 November 2018 is a particularly interesting time to analyze the portioned vertical motion fields as it falls in the middle of the period of most rapid development of this storm. We first plot the model ascent from the GFS analysis at 500 hPa (Fig. 4.4).
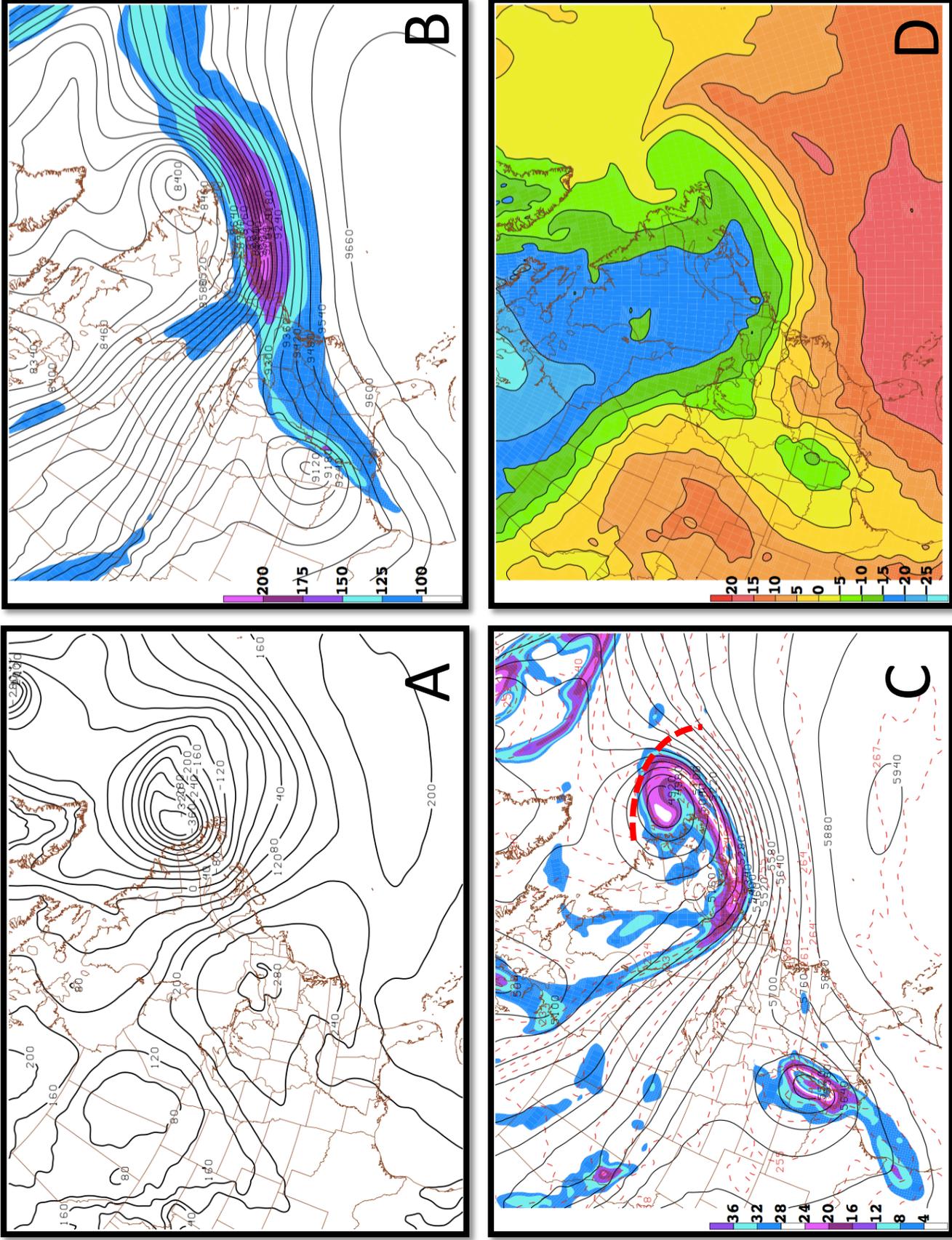
Figure 4.3: (A) 1000 hPa heights (black) every 40 m, **(B)** 300 hPa heights (black) and wind in knots (color fill), **(C)** 500 hPa heights (black), temperature every 3 degrees Kelvin (dashed contours), and positive vorticity (color fill) with inflection point (red), and **(D)** 850 temperatures (color fill) all from 15 UTC on 15 November 2018.
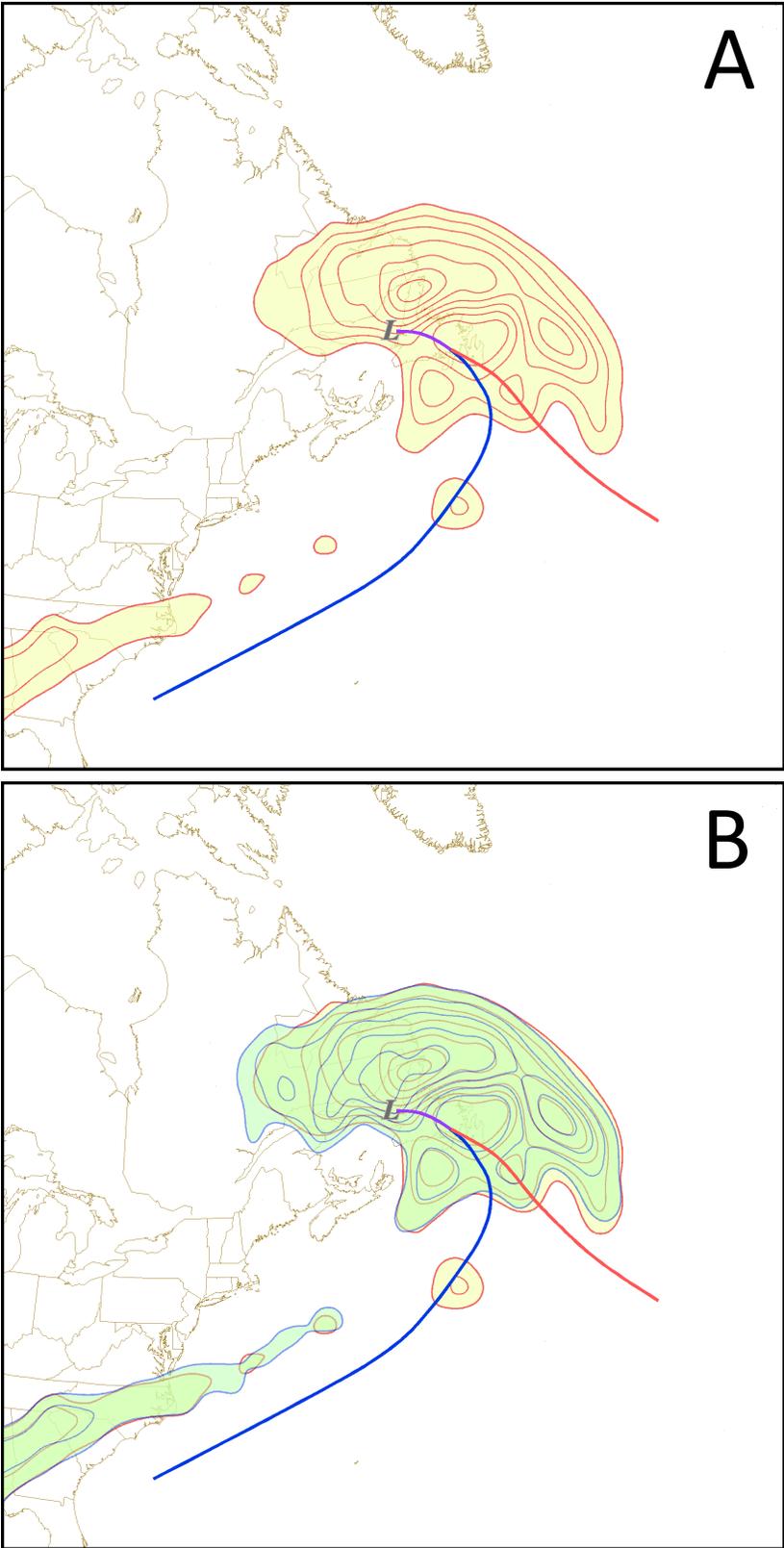
Figure 4.4: 500 hPa negative omega and fronts at 1200 UTC on 14 November 2018 **(A)** GFS analysis in yellow and **(B)** calculated kinematic omega in green.
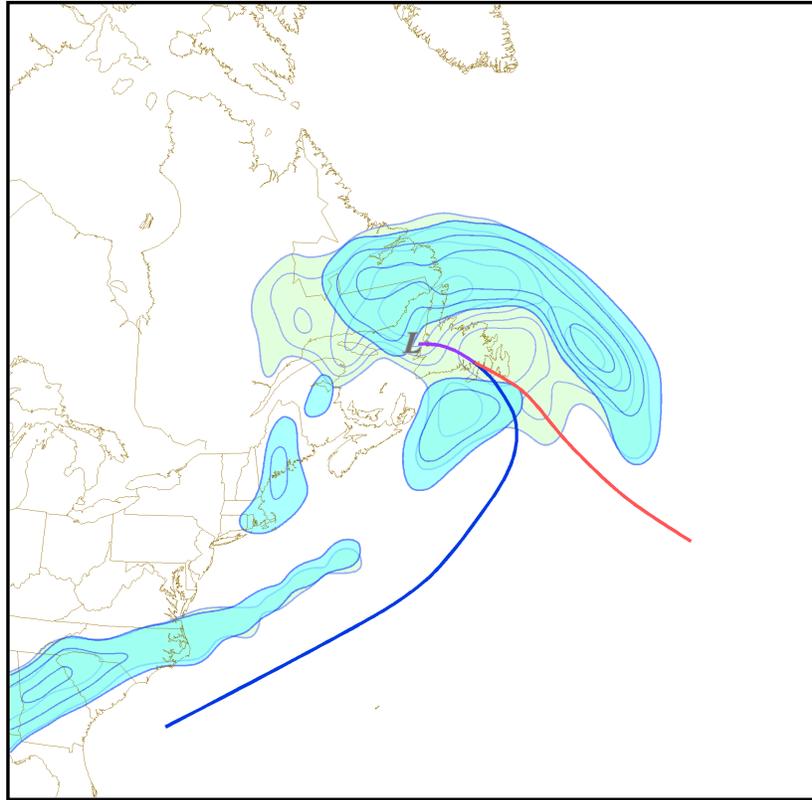
Figure 4.5: 500 hPa negative omega and fronts at 1200 UTC on 14 November 2018. The free atmosphere kinematic omega is in blue overlaying the total kinematic omega in green.

Most of the ascent is located to the north and east of the cyclone center in the direction that the cyclone is tracking (Fig. 4.4a). The modeled ascent compares very favorably to the calculated kinematic ascent in both magnitude and areal extent (Fig. 4.4b). As the vertical motion partition described in Chapter 2 requires neglect of friction, we calculate the kinematic omega associated with the integrated divergence in the "free atmosphere" (defined as everywhere above 850 hPa) and compare it to the full kinematic omega in Fig. 4.5.   Unsurprisingly, the frictionless kinematic omega is not a perfect match to the full kinematic omega. This is especially noticeable in the ascent region associated with the cloud head of the developing cyclone. Somewhat surprisingly, the 500 hPa strip of ascent associated with the cold front is nearly perfectly

accounted for by the frictionless omega. Overall, though there are regions of the mid-tropospheric omega that depend on convergence in the friction layer, there is enough similarity between the frictionless and full kinematic omegas to suggest that partitioning of the frictionless omega will provide fresh insight into the nature of the development process. Accordingly, the remainder of the analysis presented in this chapter will consider only components of the frictionless kinematic omega.

The frictionless kinematic omega can be partitioned into contributions from two species of vertical motion- one arising from speed changes and one arising from directional changes in the flow. As in any cyclogenesis case, evacuation of mass from the column is the central mechanism of rapid intensification. Application of the vertical motion partition reveals that a large portion of the upper-level ascent (i.e. mass evacuation) is associated with ageostrophy forced by a directional change in the flow, especially to the east-northeast of the cyclone center (Fig. 4.6a). The remainder of the ascent is forced by speed change ageostrophy, especially near the cold front and to the northwest of the sea level pressure minimum (Fig. 4.6b).

These relationships are summarized in schematic form in Figure 4.7. The dashed red area outlines the region of total kinematic ascent at 500 mb for this storm, along with the ascent from speed change in blue and direction change in green. This schematic highlights both the interaction and independence of the separate vertical motions that arise from the two components of ageostrophy. The ascent arising from speed change has two pieces. One is a linear feature stretched along the 500 hPa baroclinic zone associated with the cold front with a concentration near the right jet
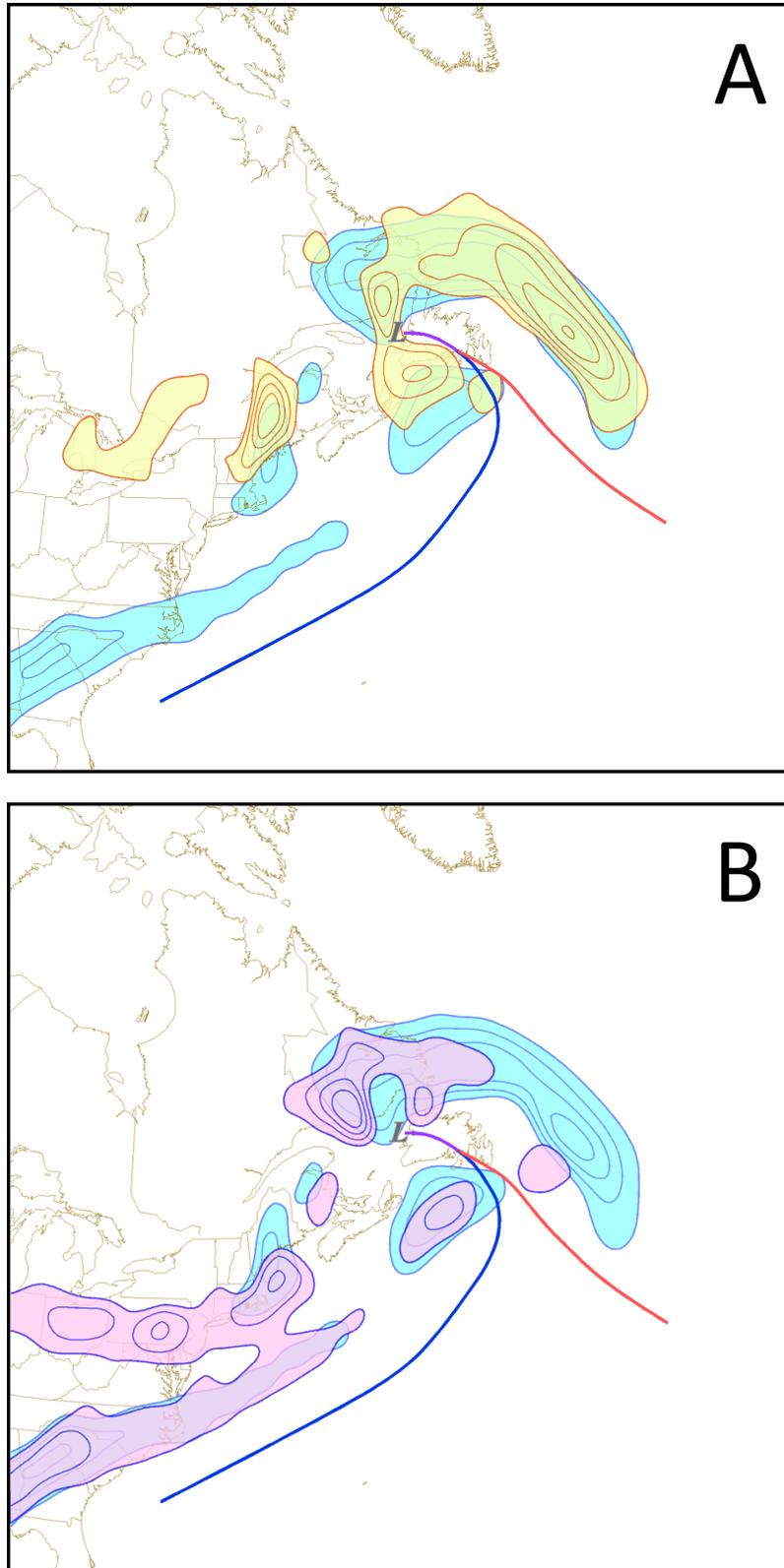
**Figure 4.6**: 500 hPa negative omega and fronts at 1200 UTC on 14 November 2018 with blue representing the kinematic omega in the free atmosphere **(A)** yellow representing the ascent from direction change and **(B)** purple representing the ascent from speed change.
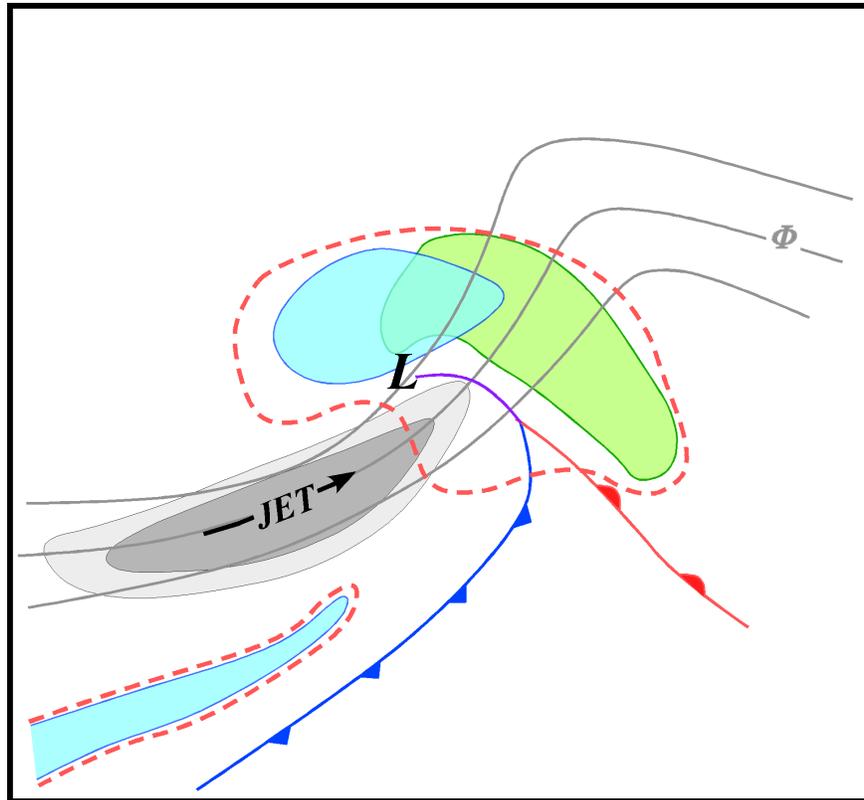
Figure 4.7: Conceptual schematic at 500 hPa with theta contours, a shaded jet streak, and fronts. The total kinematic ascent is in red, with free atmosphere speed change ascent in blue and directional change ascent in green.

entrance region. The second is a more isotropic feature near the left jet exit region that

appears to provide support for column stretching near the surface cyclone center. The

ascent induced from curvature of the flow is located downstream of the upper level

trough is aligned almost perfectly along the curved axis in Fig. 4.2b representing the

inflection point of directional change at 500 hPa. These distributions conform nicely to

theoretical expectations. Together, the two species make up a good portion of the total

kinematic ascent and even work constructively in some regions such as just NNE of the

surface low center. The unshaded portion of the red outlined region, the remainder of

the total kinematic vertical motion, is likely accounted for by frictionally induced vertical

motions.

Despite the fact that the sum of the two components of the partitioned, free

atmosphere kinematic vertical motions is precisely equal to the total, a troubling issue is

that the two components tend to have a lot of cancellation between them. For

instance, Fig. 4.8 shows that some of the ascent forced by speed change is partially

cancelled by descent forced by directional change. Similarly, some of the ascent forced

by directional change is partially cancelled by descent forced by speed change (Fig. 4.9).

To this point in the research, it is not yet physically or mathematically clear why such

cancellation between these partitioned species of vertical motions is so characteristic.
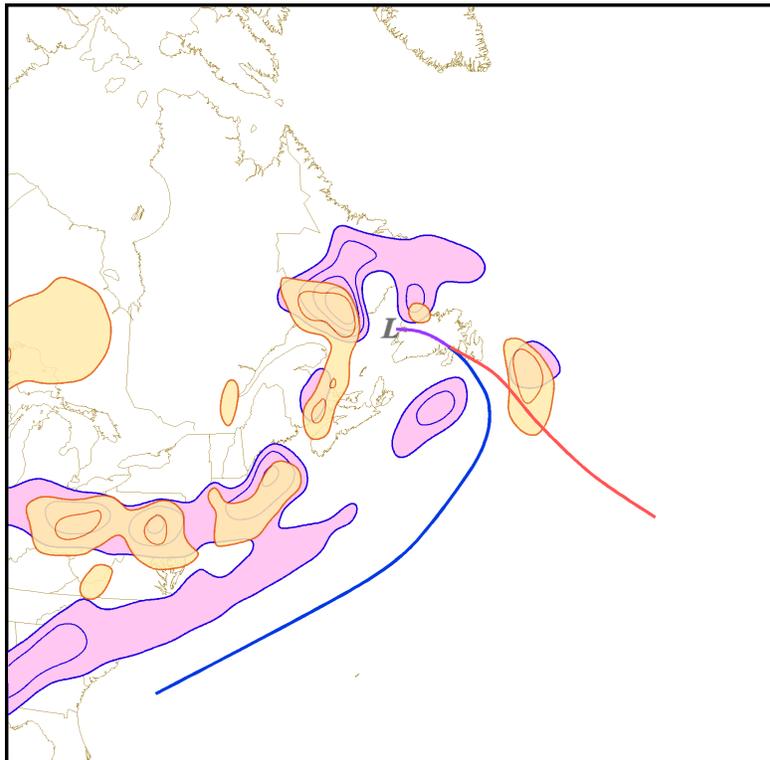
Figure 4.8: 500 hPa speed change ascent in purple and directional change descent in orange from 1200 UTC on 14 November 2018.
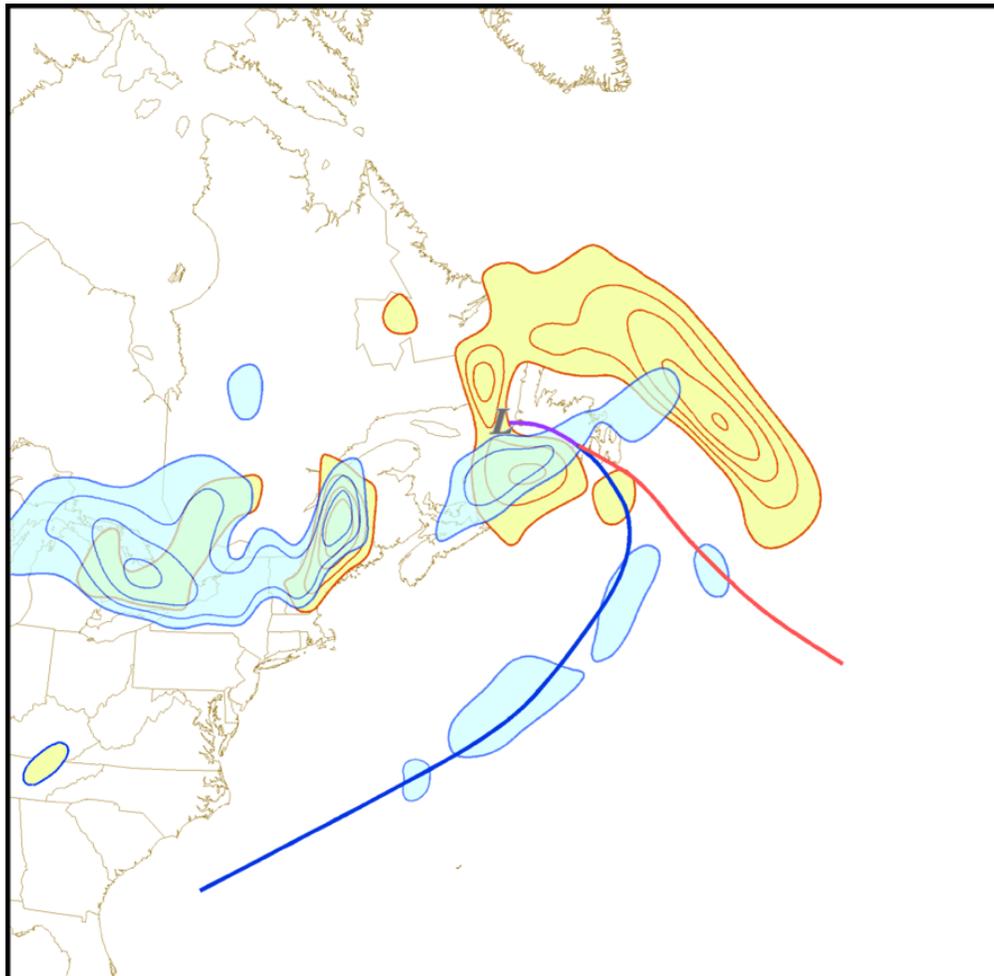
Figure 4.9: 500 hPa directional change ascent in yellow and speed change descent in blue from 1200 UTC on 14 November 2018.

5. CONCLUDING THOUGHTS

Assessment of vertical motion and diagnosis of its origin are important aspects of dynamic meteorology. Traditionally, this dual analysis is made by appealing to an approximation of one form or another, the most common one being the QG-omega equation. Even this popular approximation incorporates the fact that, at the most fundamental level, it is the 3-D distribution of ageostrophic divergence that forces synoptic-scale vertical motions. In the absence of friction, the ageostrophic wind is the portion of the total wind that arises from an acceleration of the flow and such an acceleration must be attributed to changes in either wind speed or direction. The ubiquity of curvature and along-flow speed change in the middle and upper troposphere of the middle latitudes leads to ageostrophic circulations that can work independently, in tandem, or against each other to influence synoptic-scale vertical motions. The goal of this study was to investigate a new method for analyzing the forcing for synoptic-scale vertical motions by using the current wealth of available model output and by appealing to the foregoing fundamental notions. Application of the resulting novel method of vertical motion diagnostics has led to fresh insights regarding aspects of the distribution of vertical motions in the free atmosphere.

The method begins with the frictionless, isobaric, horizontal equation of motion which dictates that a Lagrangian change in the wind vector is the result of an imbalance between the pressure gradient and Coriolis forces. This imbalance is manifest in the ageostrophic wind. After a horizontal acceleration has been isolated, the acceleration vector itself can be split into two orthogonal vectors - one representing the acceleration

arising from speed change and the other representing the acceleration arising from a directional change of the flow. Consideration of the components of acceleration along- and across the flow, it becomes apparent that the along-flow portion of the ageostrophic wind responds to directional changes while the across-flow component responds to speed changes. Employing the isobaric continuity equation, with application of an O'Brien (1970) correction, one can integrate the separate pieces of the ageostrophic wind in order to calculate orthogonal pieces of the frictionless, kinematic omega. This analysis technique was applied to two canonical developments in the mid-latitude atmosphere.

The first was analysis of the development of an upper-level front on 2 February 2018. Analysis revealed that the divergence of speed change ageostrophy was the leading forcing that contributed to the column of descent beneath the jet core that resulted in development of the upper front. However, the resulting subsidence was set in opposition to coincident ascent forced by ageostrophy associated with curvature. In fact, the ratio of speed change ageostrophy to curvature ageostrophy will change from case to case depending on the synoptic environment of the individual case. In work not presented here, it has become clear that it is not uncommon for regions of ascent in the upper troposphere caused by a directional change to directly opposes the speed change descent, or vice versa, as seen in this case study. Chapter three also compared vertical motions originating in the boundary layer (under 800 hPa) with those originating in the free atmosphere. While both play an important role in the total kinematic vertical velocity field, the method in question only partitions ageostrophy forced in the free

atmosphere. This is shown to be a valid assumption to make as the synoptic features that bring about the ageostrophy in question, such as jet streaks and Rossby wave trains, are features commonly found in the middle-to-upper troposphere above the prescribed boundary layer.

Investigation of a case of rapid cyclogenesis off the Eastern Seaboard that occurred on 14 November 2018 was also presented. The omnipresence of speed and direction change in the region of rapid development resulted in a combination of both types of ageostrophy driving ascent at 500 hPa during this event. A large portion of the upper-level ascent was associated with ageostrophy forced by a directional change in the flow, especially to the east-northeast of the cyclone center. Other portions of ascent were forced by speed change ageostrophy, especially near the cold front and to the northwest of the sea level pressure minimum. Similar to the upper front case, there were regions in which the vertical motions associated with the separate ageostrophic components destructively interfered with each other. Based on the results of this case, a conceptual model was advanced illustrating the regions of ascent forced by speed change and directional change ageostrophy for developing mid-latitude cyclones. The conceptual model highlights both the interaction and independence of the separate vertical motions that arise from the two components of ageostrophy. It also accounts for ascent in the region from frictionally induced vertical motions or cancellation between the two species, as the regions of ascent from curvature and speed change ageostrophy in the free atmosphere do not fully encompass the region of total kinematic ascent of the conceptual model.

There are nuances to employing this method that continue to make results hard to interpret at times. While the two components of the partitioned kinematic omega above 800 hPa always add up to equal the total kinematic omega above 800 hPa, there is an enigmatic cancelation between the partitioned components as well as their ascent and descent fields at any given level that has yet to be fully understood. It is yet to be determined in what capacity this method could be utilized to better understand the development of synoptic-scale structures. Further work will need to be conducted in order to explore this question, but it is certain that the method does suggest physically reasonable results, as illustrated in this thesis, that may provide new insights into fundamental forcings for synoptic-scale vertical motions in a variety of canonical developmental environments.

REFERENCES

Bjerknes, J., 1926: The structure of fronts. *Meteor. Mag.*, **61**, 32-33.

--------, 1951: Extratropical cyclones. In *Compendium of Meteor.* (pp. 577-598), Amer. Meteor. Soc., Boston, MA., https://doi.org/10.1007/978-1-940033-70-9_48.

--------, and J. Holmboe, 1944: On the theory of cyclones. *J. Meteor.*, **1**, 1, 1–22, https://doi.org/10.1175/1520-0469(1944)001<0001:OTTOC>2.0.CO;2.

--------, and E. Palmen, 1937: Investigation of selected European cyclones by means of serial wscents. *Am. Meteorol. Soc.,* **12**, 66.

--------, and H. Solberg, 1922: Life cycles of cyclones and the polar front theory of atmospheric circulation. *Geofys. Publ.*, **3**, 1-18.

Bushby, F. H., 1952: The evaluation of vertical velocity and thickness tendency from Sutcliffe's theory. *Quart. J. Roy. Meteor. Soc.*, **78**, 337, 354–362, https://doi.org/10.1002/qj.49707833705.

Charney, J.G., 1948: On the scale of atmospheric turbulence. *Geofys, Publikasjoner, Norske Videnskaps-Akad. Oslo,* **17**, 3.

desJardins, M. L., & R. A. Petersen, 1983: GEMPAK: An interactive meteorological display and analysis system. Preprints. In *Ninth Conf. on Aerospace and Aeronautical Meteor.,* 55-59 pp.

Dines, W. H., 1914: Cyclones and anticyclones. *J. Scot. Meteor, Soc.,* **16**, 304-311.

Eliassen, A., 1949: The quasi-static equations of motion with pressure as independent variable. *Grøndahl & sons boktr., I kommisjon hos Cammermeyers boghandel*.

--------, 1962: On the vertical circulation in frontal zones. *Geofys. Publ.,* **24**, 4, 147-160.

Fjørtoft, R., 1955: On the use of space-smoothing in physical weather forecasting. *Tellus*, **7**, 4, 462–480, https://doi.org/10.1111/j.2153-3490.1955.tb01185.x.

Hoskins, B. J., I. Draghici, and H.C. Davies, 1978: A new look at the ω-equation. *Quart. J. Roy. Meteor. Soc.*, **104**, 439, 31–38, https://doi.org/10.1002/qj.49710443903.

Keyser, D., & M. A. Shapiro, 1986: A review of the structure and dynamics of upper-level frontal zones. *Mon. Wea. Rev.*, **114**, 2, 452–499, https://doi.org/10.1175/1520-0493(1986)114<0452:AROTSA>2.0.CO;2.

Martin, J. E., 2014: Quasi-geostrophic diagnosis of the influence of vorticity advection on the development of upper level jet-front systems. *Quart. J. Roy. Meteor. Soc.*, **140**, 685, 2658–2671, https://doi.org/10.1002/qj.2333.

Mudrick, S. E., 1974: A numerical study of frontogenesis. *J. Atmos. Sci.,* **31**, 4, 869-892, https://doi.org/10.1175/1520-0469(1974)031<0869:ANSOF>2.0.CO;2.

Namis, J., and P. F. Clapp, 1949: Confluence theory of high tropospheric jet stream. *J. Meteor.,* **6**, 330-336.

National Centers for Environmental Prediction/National Weather Service/NOAA/U.S. Department of Commerce, 2007: NCEP Global Forecast System (GFS) Analyses and Forecasts. Research Data Archive at the National Center for Atmospheric

Research, Computational and Information Systems Laboratory, Boulder, CO.
[Available online at https://doi.org/10.5065/D65Q4TSG.]

O'Brien, J. J., 1970: Alternative solutions to the classical vertical velocity problem. *J. Appl. Meteor.*, **9**, 2, 197–203, https://doi.org/10.1175/1520-0450(1970)009<0197:ASTTCV>2.0.CO;2.

Palmén, E., 1948: On the distribution of temperature and wind in the upper westerlies. *J. Meteor.*, **5**, 1, 20–27, https://doi.org/10.1175/1520-0469(1948)005<0020:OTDOTA>2.0.CO;2.

--------, and K. M. Nagler, 1949: The formation and structure of a large-scale disturbance in the westerlies. *J. Meteor.*, **6**, 4, 228–242, https://doi.org/10.1175/1520-0469(1949)006<0228:TFASOA>2.0.CO;2.

Petterssen, S., and S. J. Smebye, 1971: On the development of extratropical cyclones. *Quart. J. Roy. Meteor. Soc.*, **97**, 414, 457–482, https://doi.org/10.1002/qj.49709741407.

Reed, R. J., 1955: A study of a characteristic type of upper-level frontogenesis. *J. Meteor.*, **12**, 3, 226–237, https://doi.org/10.1175/1520-0469(1955)012<0226:ASOACT>2.0.CO;2.

--------, and F. Sanders, 1953: An investagation of the development of a mid-tropospheric frontal zone and its associated vorticity field. *J. Meteor*, **10**, 5, 338–349, https://doi.org/10.1175/1520-0469(1953)010<0338:AIOTDO>2.0.CO;2.

Rotunno, R., W. C. Skamarock, and C. Snyder, 1994: An analysis of frontogenesis in numerical simulations of baroclinic waves. *J. Atmos. Sci.*, **51**, 23, 3373–3398, https://doi.org/10.1175/1520-0469(1994)051<3373:AAOFIN>2.0.CO;2.

Sawyer, J. S., 1956: The vertical circulation at meteorological fronts and its relation to frontogenesis. *Proceedings of the Royal Society of London. Series A. Mathematical and Physical Sciences*, **234**, 1198, 346-362. https://doi.org/10.1098/rspa.1956.0039.

Scherhag, R., 1934: Zur theorie der hochund tiefdruckgebiete. *Meteor. Z,* **51**, 129-138.

Shapiro, M. A., 1981: Frontogenesis and geostrophically forced secondary circulations in the vicinity of jet stream-frontal zone systems. *J. Atmos. Sci.*, **38**, 5, 954–973, https://doi.org/10.1175/1520-0469(1981)038<0954:FAGFSC>2.0.CO;2.

--------, 1983: Mesoscale weather systems of the central United States. In *The National STORM Program: Scientific and Technological Bases and Major Objectives,* Athens RA (ed.): 3.1-3.77. University Corporation for Atmospheric Research: Boulder, CO.

--------, and P. J. Kennedy, 1981: Research aircraft measurements of jet stream geostrophic and ageostrophic winds. *J. Atmos. Sci.*, **38**, 12, 2642–2652. https://doi.org/10.1175/1520-0469(1981)038<2642:RAMOJS>2.0.CO;2.

Sutcliffe, R. C., 1938: On development in the field of barometric pressure. *Quart. J. Roy. Meteor. Soc.*, **64**, 276, 276, 495–509, https://doi.org/10.1002/qj.49706427614.

--------, 1939: Cyclonic and anticyclonic development. *Quart. J. Roy. Meteor. Soc.*, **65,** 282, 518–524, https://doi.org/10.1002/qj.49706528208.

--------, 1947: A contribution to the problem of development. *Quart. J. Roy. Meteor. Soc.*, **73**, 317–318, 370–383, https://doi.org/10.1002/qj.49707331710.

Thompson, P. D., 1961: Numerical weather analysis and prediction. *The Macmillan Co.*, 170 pp.